Members of the Ph.D. committee are satisfied with the presentation and recommended for submission for Ph.D. thesis in due time

DEFORMATION, METAMORPHISM AND GEOCHRONOLOGICAL EVOLUTION OF THE HIGH-GRADE PROTEROZOIC ROCKS AROUND BOUDH, ODISHA: IMPLICATIONS ON DEVELOPMENT OF STRUCTURAL-KINEMATIC DOMAINS AND ASSEMBLY OF THE NORTHERN EASTERN GHATS BELT.

28/11/24 28/11/2024 28/11/24

Summary

By

Shuvankar Karmakar

Abijit Ray 28/11/24

Shuvankar Karmakar

Registration No.: R-18RS215170197

PRESIDENCY UNIVERSITY
KOLKATA

28/11/24 Supervisor

Dr. Gautam Ghosh & Dr. Sankar Bose

2024

Scanned with OKEN Scanner

1. INTRODUCTION

Granulite facies rocks in Proterozoic orogenic belts provide valuable insights into the deformation behaviour and evolution of the lower crust. These regions typically document rock records of assembly and breakup of ancient supercontinents (Cawood et al., 2009 and references there in) and their evolutionary history. The geological works on such mobile belts had been mostly focused on petrological, geochronological, fluid and isotopic aspects of the rocks while the deformation history manifested by the high-grade rock suite remains lesser studied to date. Therefore, integrating deformation analysis with petrochronology can enhance our understanding of the lower crustal rheology and geodynamic processes. Examples of few such integrated studies include the Moine Supergroup in Scotland (Alsop and Holdsworth, 2006; Strachan et al., 2010), the Pan-African Wadi Hafafit in Egypt (Abd El-Naby et al., 2008), the Namaqua belt in southern Africa (Colliston et al., 1991), and the Ribeira belt in Brazil (Faleiros et al. 2011, 2016), where detailed works have revealed complex, multi-phase deformation histories that helped in constraining the kinematic evolutionary models for such belts.

The Eastern Ghats Belt (EGB) skirting the east coast of India, represents a complex, polydeformed polymetamorphosed terrane and is considered a type area for examining Proterozoic crustal processes and terrane accretion models (Lal et.al. 1987, Sengupta et. al. 1990; Dobmeir and Raith, 2003; Upadhyay et al., 2009; Das et al., 2011; Korhonen et al., 2013b; Sarkar and Schenk, 2016; Dasgupta et al., 2017; Bose, 2020; Dasgupta, 2020). The records of assembly and dispersal of Proterozoic supercontinents are believed to be well preserved in the rocks of the EGB (Bose et. al., 2011; Dasgupta et. al. 2013). However, compared to the petrological, geochronological and metamorphic works on the EGB (Bose, 2020; Dasgupta, 2020 and references therein), structural studies are comparatively less and mostly focused along the contact zones of the EGB with the neighbouring cratons (Bhattacharya and Gupta, 2001; Bhadra et al., 2004; Biswal et al., 2007; Kar, 2007; Sarkar et al., 2007; Das et al., 2008; Chetty, 2014; Ghosh et al., 2010b, 2016). Few studies on structural evolution have been attempted from the interior parts of the EGB (Bhowmik, 1997; Das et al., 2011, 2012; Saha and Karmakar, 2015), but data on deformation kinematics, geochronology and metamorphic history from the northern margin of this belt (contact of the EGB with the Rengali Province-Singhbhum Craton) is poorly understood till date. The present work is focused on studying the deformation-metamorphic history of the granulite

facies rocks around Boudhgarh, Odisha in northern EGB, to develop a tectonometamorphic evolutionary model of the belt, particularly in the context of the Rayner-Eastern Ghats orogeny and its role behind amalgamation of India with East Antarctica.

2. GEOLOGICAL BACKGROUND

The EGB consists of granulite facies rocks that experienced ultra-high temperature (UHT) metamorphism (> 900°C at 7–10 kbar) during the late Mesoproterozoic time (Bose, 2020; Dasgupta, 2020 and references therein). Initially classified into lithology based longitudinal zones (Ramakrishnan et al., 1998), it was later sub-divided into several crustal provinces and domains based on Nd-model ages and distinct geological histories (Rickers et al., 2001; Dobmeier and Raith, 2003). Amongst the provinces, the northern Eastern Ghats Province (EGP) bears a younger (< 1.0 Ga) metamorphic history, while the southern Krishna Province is older (> 1.5 Ga). The Jeypore and Rengali Provinces outcrop bordering the Bastar and Singhbhum Cratons respectively and show Archaean metamorphic and geochronological traits (Dobmeier and Raith, 2003; Bose et al., 2016).

The Visakhapatnam domain in the EGP experienced UHT metamorphism (T>950°C at 8–10 kbar; Lal et al., 1987; Sengupta et al., 1990; Dasgupta et al., 1995; Pal and Bose, 1997; Bose and Das, 2006; Bose et al., 2000, 2006, 2016, 2022; Das et al., 2006a, 2011, 2017; Korhonen et al., 2013a) with an anticlockwise P-T path around 1000–900 Ma (Upadhyay et al., 2009; Bose et al., 2011; Das et al., 2011; Korhonen et al., 2013b). The peak UHT metamorphism was reached at ~ 1000°C, 8 kbar during ca. 1030-990 Ma and a retrograde history is characterized by near-isobaric cooling down to 800°C (reviewed in Bhowmik et al., 2024). Bose et al. (2022) established two separate tectonometamorphic cycles from monazite petrochronology of aluminous granulites of the EGP; the first cycle (M_1) spanned about 40 million years (ca. 1030-990 Ma) when the rock was metamorphosed to UHT condition (~ 1000°C, 8 kbar) through a counterclockwise P-T path followed by near-isobaric cooling. The second cycle (M_2) spanned about 50 million years (ca. 950-900 Ma) when the cooled lower crust reworked through a clockwise P-T path due to a compressional event. These two pulses were accompanied by voluminous arc magma now represented by charnockite massif (Mondal et al. 2023); an early magmatic pulse (ca. 1020-1000 Ma) was coeval with M_1 UHT metamorphism while a more prominent later magmatic pulse occurred at ca. 980-940 Ma.

Ganguly et al. (2021) carried out a detailed structural study from the Phulbani domain in the northern EGP to unravel five deformation phases (D_1-D_5). The domain experienced peak UHT metamorphism (850°C-1000°C, 8.0-8.5 kbar) with an anticlockwise P-T path around ca. 987-970 Ma (Ganguly et al., 2017, 2018). Geological data from the nearby Rampur-Khariar (Fig. 1) domains remain scarce till date. The Rampur-Khariar domains lie at the EGP's northwest boundary with the Bastar Craton, which is typically described as a thrust boundary, referred to as the Eastern Ghats Boundary Shear Zone (EGBSZ; Ramakrishnan et al., 1998) or Terrane Boundary Shear Zone (TBSZ Bhadra et al., 2004; Biswal et al., 2007), with a splay as the Sileru Shear Zone (SSZ) in its hanging wall side (Fig. 1). The TBSZ shows a major tectonothermal reworking at ca. 520-500 Ma coeval with the Kuunga Orogeny, interpreted to be the timing of amalgamation of Bastar craton with the EGP (Biswal et al. 2007; Simmat and Raith, 2008; Chatterjee et al. 2017a, b; Ranjan et al. 2018 and references therein). Recent studies by Padmaja et al. (2021, 2022, 2024) from the Deobhog area show a clockwise P-T path of evolution with a decompression-dominated retrograde history. Based on monazite geochronology, they considered orogenic activity along the TBSZ to take place during early Neoproterozoic. Recent studies from the Angul domain by Banerjee et al. (2023) reported two-stage evolutionary history in which the early metamorphic event occured at a peak of ~ 850°C, 7-8 kbar during ca. 1200 Ma and the later event at ca. 990-960 Ma with a counter-clockwise P-T path at ~ 800°C, 4.0-8.5 kbar. From the absence of ca. 1200 Ma metamorphic event from the rest of the EGP, these authors considered the Angul domain as an exotic block and correlated it with the Prydz Bay region of East Antarctica.

The northern EGP is characterized by crustal-scale faults or shear zones (Mahalik, 1994; Crowe et al., 2003; Dobmeier and Raith, 2003; Fig. 1) like the Kerajang Fault Zone (KFZ; Ghosh et al., 2016), Mahanadi Shear Zone (MSZ; Chetty, 2001; Mahapatra et. al. 2009; Bose and Gupta, 2018, 2020; Bose et al., 2019), and Ranipathar Shear Zone (RSZ; Crowe et al., 2003; Chetty, 2010; Ganguly et al., 2017, 2018). The latter merges due west with the N-NNW striking Nagavalli-Vamshadhara Shear Zone (NVSZ; Dobmeier and Raith, 2003; Saha and Karmakar, 2015). Chetty (2014) identified a crustal-scale positive flower structure in the northern contact zone, while Ghosh et al. (2016) noted transpressional features in the Rengali Province, which are distinct from the thrust-dominated western EGB. Mahapatra et al. (2009) linked the MSZ to extensional tectonics, while Bose and Gupta (2018, 2020) and Bose et al.

(2019) reported two shearing events. Saha and Karmakar (2015) found four stages of deformation and a transpressive setting in the NVSZ.

The present study focuses on the Boudhgarh area in Odisha, located at the tri-junction of the Phulbani, Tikarpara, and Khairiar domains, intersected by the MSZ, RSZ, and NVSZ, to address gaps in knowledge and explore issues related to the evolution of the EGP in the broad framework of Proterozoic supercontinent assembly.

3. OBJECTIVE

1. Disentangling the deformation history of the proposed study area and its correlation with neighbouring domains of the EGP.
2. Mapping the extent of the MSZ and RSZ in the study area and establishing their kinematics.
3. A comparative study of the deformation history of the MSZ-RSZ and intervening domains from the study area.
4. Study of strain variation, P-T estimation and vorticity pattern in the study area vis-à-vis the bounding crustal-scale shear zones.
5. Deciphering the metamorphic imprints and their correlation with deformation phases in the study area.
6. Geochronological studies to constraint the timings of major tectonometamorphic events in the study area.
7. Deciphering rheology and flow behaviour of the granulite facies rocks under lower crustal conditions and during subsequent exhumation.
8. Developing a tectono-evolutionary model of the northern EGB using data assimilated from the study area and its possible correlation with the global Proterozoic supercontinent cycles.

4. METHODOLOGY

1. A total of 150 thin sections were studied with a polarizing microscope and JEOL JSM IT500 Scanning electron microscope (SEM) at Presidency University. Selected finer mineral phases were analyzed using an Energy Dispersive Spectrometer (EDS) attached to the SEM while Backscattered Electron (BSE) images were produced using a BSE detector attached to the same SEM.

2. Chemical data for representative samples of the mafic granulite, aluminous granulite, felsic gneiss, calc-silicate granulite, hornblendite and hornblende gneiss were obtained using a CAMECA SXFive tactis electron microprobe analyzer (EPMA) at the National Centre for Earth Science Studies (NCESS), Thiruvananthapuram, India. The analytical protocol for the instrument was followed after Sorcar et al. (2021). Ti-in-quartz was determined by the same CAMECA SXFive tactis EPMA at NCESS.
3. Whole rock major, trace, and rare earth element (REE) data from representative samples of mafic granulites, felsic gneiss, hornblendite and hornblende gneiss were analyzed at the Australian Laboratory Services Pty. Ltd., Brisbane, Australia. The analysis was done using ICP-AES for the whole rock package (ME-ICP06) and Lithium Borate Fusion ICP-MS (ME-MS81). Processing and plotting of data were done using the GCDkit program (Janoušek et al., 2006).
4. Zircon U-Pb analyses were carried out using the LA-ICPMS facility at Hiroshima University, Japan following the methods described in Katsube et al. (2012) and Das et al. (2017). Monazite grains were analyzed by CAMECA SX Five tactis EPMA at the NCESS for U-Th-total Pb dating. The detailed method followed was after Sorcar et al. (2021).
5. Quantitative 3D and 2D finite strain analysis were performed using SPO software (Launeau and Robin, 2003) and ELLIPSOID software (Launeau and Robin, 2003, 2005) and strain data were plotted in Flinn's diagram (Flinn, 1962) and Hossack's diagram (1968).
6. Different methods were used to determine the vorticity using (i) Porphyroclast Aspect Ratio (PAR; Passchier, 1987a; Wallis, 1995) and (ii) Oblique Grain Shape Fabric (δ/β and R_{XZ}/β) techniques (Xypolias and Koukouvelas, 2001; Xypolias, 2009; Law, 2010).
7. The EBSD patterns were acquired using the Nordlys system attached to the scanning electron microscope (SEM) JEOL JSM6390A at the Department of Earth and Planetary Science, Hiroshima University, Japan which was run with an accelerating voltage of 15 kV and sample tilt of 70°. Additionally, the Nordlys system attached with SEM JEOL JSM IT500 installed at the Department of Geology, Presidency University, Kolkata was also used for acquiring EBSD data.

5. GEOLOGY OF THE STUDY AREA

The study area around Boudhgarh lies in between the MSZ and the RSZ in northern EGP (Fig. 1). The WNW-ESE trending MSZ separates the Phulbani domain from the Angul-Tikarpara domain (Fig. 1). The MSZ has been investigated by several studies (Mahapatro et al., 2009; Bose and Gupta, 2018; Ghosh et al., 2021). The E-W trending RSZ marks the southern boundary of the area merging with the MSZ forming a Y-shaped junction. The study area has been divided into three domains: Lithostructural domain (LSD-1) incorporates the Mahanadi Shear Zone, Lithostructural domain (LSD-2) – the area bounded in the north by MSZ and in the south by RSZ and Lithostructural domain (LSD-3) incorporates RSZ (Fig. 2). A descriptive summary of the samples locations, mineral assemblages, textural features and calculated ages are presented in Table 1.

Lithostructural domain (LSD 1) (Mahanadi Shear Zone)

The major rock type is mylonitic augen gneiss (quartz + plagioclase + K-feldspar + gernet + ilmenite + biotite) containing large feldspar augen (Fig. 3a). Locally, enclaves of mylonitic felsic gneiss (Fig. 3b) defined by alternate quartz + feldspar-rich leucocratic and garnet+ biotite-rich melanocratic layers are present within mylonitic augen gneiss (Fig. 3c). Deformed enclaves (few centimetres to few meters) and lenses of orthopyroxene granulite (orthopyroxene+ plagioclase+ hornblende + biotite+ ilmenite; Fig. 3d), clinopyroxene+ titanite bearing mafic granulite (biotite+ plagioclase+ hornblende+ clinopyroxene+ titanite+ quartz+ ilmenite), hornblendite (hornblende + plagioclase + K-feldspar + quartz + titanite + ilmenite) and hornblende gneiss (quartz + plagioclase + hornblende + garnet + K-feldspar + ilmenite) are present within the mylonitic felsic gneiss. A few smaller enclaves (up to a few tens of centimetres in size) of garnet + clinopyroxene-bearing mafic granulite (garnet + clinopyroxene + plagioclase + quartz + orthopyroxene + hornblende + biotite + rutile + ilmenite) occur within the felsic gneiss and the orthopyroxene granulite (Fig. 3e, f).

Lithostructural domain (LSD 2) (MSZ Footwall)

The dominant host rock is felsic rock and coarse-grained charnockite (quartz + K-feldspar + plagioclase + orthopyroxene + garnet + biotite + ilmenite). The felsic rock is mostly porphyritic granite with local development of crude foliation, defined by elongated feldspar porphyroclasts. The charnockite is coarse-grained and massive to weakly foliated (gneissic) in character. Enclaves of two-pyroxene granulite (orthopyroxene+ clinopyroxene+

plagioclase+ ilmenite+ quartz), garnet + orthopyroxene-bearing granulite (plagioclase+ garnet+ orthopyroxene+ K-feldspar+ biotite+ ilmenite; Fig. 3g) and calc-silicate granulite (quartz + plagioclase + K-feldspar + clinopyroxene + titanite + garnet + wollastonite + calcite + ilmenite; Fig. 3h) occur within charnockite. On the other hand, the felsic gneiss contains enclaves of garnet + orthopyroxene-bearing mafic granulite and aluminous granulite (garnet + spinel + sillimanite + quartz + biotite + ilmenite).

Lithostructural domain (LSD 3) (Ranipathar Shear Zone)

The dominant rock types include migmatitic felsic gneiss which hosts aluminous granulite, coarse- and fine-grained charnockite, felsic augen gneiss, and mafic granulite. Aluminous and mafic granulites form enclaves within the migmatitic felsic gneiss, while intrusive coarse-grained charnockite contains granulite enclaves. A NW-SE gneissic fabric in the south is folded and overprinted by the E-W mylonitic fabric along RSZ indicating dextral strike-slip shearing. The mylonitic foliation is oriented 275°/78°N, with a lineation plunging 73° towards 015° (Fig. 2a).

6. STRUCTURAL ANALYSIS

Detailed structural analysis has been carried out from LSD-2 and LSD-1 in the present study. Further based on outcrop-based structural data, the southern boundary of the MSZ has been denoted as LSD-1a while the interior part has been denoted as LSD-1b.

Phulbani domain (LSD-2)

The earliest recognizable fabric S_1 is preserved in the enclave suite of rocks (Fig. 4a; Table 1). Intermittent occurrence of the enclave suite rocks in the central part of the area defines a map scale NNW trending large F_2 fold (Fig. 2) with S_1 layering serving as a form surface of the fold (Fig. 4b). Plotting of S_1 poles defines a moderately NW plunging (43°→344°; Fig. 2b) F_2 axis. The sub-vertical NNW trending S_2 foliation has developed axial planar to the large F_2 fold (343°/82°E, Fig. 2c) and can be traced in the enclave suite as well as in the host porphyritic granite (Fig. 4c). The two limbs of the F2 fold are sub-parallel to the NNW axial trace and dip ENE, forming an overturned isoclinal geometry (Figs. 2, 2h). The isoclinal folding caused S_1 foliations on both limbs to become sub-parallel to the axial planar S_2 foliation, forming a composite S_{1-2} foliation, which is predominant in this domain, excepting at the F_2 hinge where both foliations are distinct. The dominant NNW'ly azimuth of the S_2

planes changes in the northern part of the area as the MSZ is approached and becomes NW-WNW in the west to N-NNE in the east with variable dips (Fig. 2). Plotting of the S_2 plane poles gives a great circle distribution in stereoplots indicating warping with β axes plunging variably due E-ESE at steep to moderate angles (66°→115° to 59°→088°; Figs. 2d, 2e). Mylonitic foliation S_3 of variable orientations (262°/ 86°N; 346°/ 70°E; Fig. 2f) has developed locally within the domain transecting earlier foliations and is confined within a conjugate pair of mesoscopic shear zones (E-W dextral and NNW-SSE sinistral). The E-W shear zone developed in porphyritic granite gneiss, forming mylonitic augen gneiss with steep northerly dipping foliation, grading into ultramylonite bands at places (Fig. 4d). Dextral shear is indicated by sigma-shaped feldspar augen tails, asymmetric folds, and boudins in deformed quartz veins. (Fig. 4e). Folded enclaves of felsic gneiss are common within this shear zone (Fig. 4f). The NNW shear zone in mylonitized augen gneiss dips steeply east, with feldspar augen tails indicating sinistral slip.

MSZ (LSD-1a)

Along the southern boundary of MSZ, the NW to NNE trending S_2 foliation gets rotated to the MSZ trend and develops crenulations in outcrop scale. A mylonitic foliation S_{3M} develops axial planar to the crenulations and transposes the S_2 fabric. The mylonitic foliation in MSZ is labelled S_{3M} to distinguish it from S_3 in LSD-2, as their relationship couldn't be determined from field studies. A large-scale map of the contact zone depicts the deformed S_2 foliation in augen gneiss and its transposition by S_{3M} (Fig. 5). The S_2 foliation shows asymmetric fold (F_3) development with NE striking long southern limb, N-S trending, east-dipping hinge and E-W trending short northern limb (Fig.6a). From west to east, the F_3 fold axes plunge variably (39°→099°, 34°→077° to 38°→092° Figs. 5a-c) indicating their overall non-cylindrical geometry. Asymmetric crenulations form due to S_{3M} mylonitic foliation shows dextral slip (Fig. 6b). A set of NNE to NNW trending sinistral shear band ($C^{//}$) structures (028°/ 90°) have preferentially affected the E-W trending northern limb resulting in asymmetric kinks on outcrop scale (Figs. 5d, 6c). North of this fold zone, within MSZ, the S_{3M} foliation (C-fabric) is dominant trending E-W and is sub-vertical to steep north dipping (269°/ 87°N; Fig. 5e).

MSZ (LSD-1b)

The MSZ in the study area poses a broad uniformity of character, with a north dipping mylonitic foliation (S_{3M}; 287°/ 46°N; Fig. 2g) and a down-dip to low westerly plunging mineral lineation (L_{3M}; 33°→334°; Fig. 2g). Within MSZ, the deformation is extremely heterogenous due to the occurrence of alternate mylonite-ultramylonite bands and C-fabric (both S-C fabric and C$^{/}$; Figs. 6d, 6e) zones and zones where folds of different geometries and generations prevail. The *C-fabric zones* characterize the two boundaries of the MSZ as well as are present internally within it at several locales across its width. Both the strike and dip of the S_{3M} foliation in the *C-fabric zones* vary; it is dominantly E-W trending, sub-vertical to steeply north dipping along major length segments of the MSZ southern boundary (mean S_{3M} foliation, 269°/ 70-87° N). At the northern margin, the S_{3M} is characteristically gently north dipping (mean S_{3M} foliation, 265°/ 28° N with mean L_{3M} 25° → 326°) while in between, it is E-W to WNW striking with moderate to steep northerly dips (Fig. 2). The S-C structures in these zones ubiquitously point to dextral slip displacement on plan while in sections, consistently suggest a top-to-south movement on north dipping C-planes. C$^{/}$ shear bands displace C planes on plan and are consistent with dextral slip displacement. Dextral folding of C-planes on plan and development of asymmetric south verging flexures of C-planes in section are also commonly observed in these zones.

The mesoscopic folds observed in the *fold zones* has been subdivided into the following geometrically distinct groups: (1) dismembered rootless folds with axial surface parallel to the shear zone trend and hinges that rake 50° to 90° on the axial surface, (2) folds with axial plane strike parallel to the shear zone and hinges being sub-horizontal to plunging (rake 10° to 40° on axial surface), (3) multiply deformed folds portraying type 1-3 interference patterns (Ramsay, 1962) to more complex geometries, (4) asymmetric south verging flexures in section and (5) asymmetric dextral folds on plan with axial plane strike parallel to the shear zone and variably plunging hinges.

Grain-scale analysis confirms presence of two fabric zones in MSZ. The early high-temperature mylonitic fabric (S_{3MH}) is transposed by a later low-temperature fabric (S_{3ML}), details are provided in Table 2. The S-C fabric in XZ sections of S_{3MH} fabric domains in augen gneiss is defined by hornblende and type II garnet. Type I garnet grains are generally stretched (Fig. 7a), with some showing top-to-the-south reverse shear in XZ sections (Fig. 7b). K-feldspar in felsic gneiss and coarse hornblende in Cpx-Ttn-bearing mafic granulite also exhibit top-to-the-south shear sense (Figs. 7c, d), while K-feldspar grains in YZ sections

show dextral shear sense (Fig. 7e). Type II garnet clusters and hornblende display dextral shear sense in YZ sections (Fig. 7f). In augen gneiss, the low-temperature mylonitic fabric (S_{3ML}) is defined by biotite and dynamically recrystallized quartz-feldspar grains. Plagioclase and K-feldspar are altered to biotite-chlorite, with quartz showing core-and-mantle structures and SGR recrystallization. S-C fabric is defined by chlorite grains cross-cutting high-temperature fabric (Fig. 7g). In mafic granulite, S_{3ML} is marked by biotite and recrystallized quartz-feldspar aggregates, with C and S fabrics cutting across stretched clinopyroxene-titanite grains show top-to-the-south shear sense in XZ sections (Fig. 7h).

7. PETROGRAPHY AND MINERAL CHEMISTRY

LSD-1

Grt-Cpx-bearing mafic granulite (samples BDH 155D, BDH 48 and BDH 3A): The coarse granoblastic peak M_1 assemblage of Grt_2 + Cpx_2 + Pl_2 + Qtz_2 + Ilm_2 ± Rt ± Opx (Figs. 8a, b) on which Hbl_3 and Bt_3 occur as coarse patches and flakes in BDH 155D and as secondary patches in BDH 48. The porphyroblastic garnet Grt_2 contains elliptical to rounded inclusions of Pl_1, Hbl_1, Cpx_1, Ilm_1 and occasionally Rt_1 (Figs. 8a, c). Retrograde M_{1R} assemblage is identified by patches of Hbl_3 develop on Grt_2 and Cpx_2 in the presence of a H_2O-rich fluid in BDH 155D whereas in BHD 48 retrograde M_{1R} is characterised by fine-grained symplectite of Cpx_3, Pl_3 with or without Opx_3 (Fig. 8d).

Orthopyroxene granulite (sample BDH 155B): The M_1 assemblage comprises of Opx_2 and Pl_2, which occur in alternate layers that define the gneissic foliation. Secondary Hbl_3 (M_{1R}) appears to replace Opx_2 along the foliation. A few Hbl_3 grains show breakdown to dusty intergrowth of Pl_3 and Opx_3 along the margin (Fig. 8e).

Hornblendite and Hornblende gneiss (sample BDH 77B and T69): Hbl_2 and Pl_2 grains show localized recrystallization, with Ttn grains dispersed in Hbl_2 layers forming a reaction corona (Ttn_3) around small xenoblastic Ilm_2 grains (Fig. 8f). The hornblende gneiss (T69) shows a gneissic foliation shown by alternate Grt_2 + Hbl_2 (melanocratic) and Qtz_2 + Kfs_2 + Pl_2 (leucocratic) layers (Fig. 8g). Minerals in the leucocratic layer are recrystallized with polygonal boundaries. Locally Qtz_2 grains are flattened to form a ribbon structure. Grt_2 grains are locally poikiloblastic containing inclusions of Qtz_2 and Ilm_2.

Felsic gneiss-Augen gneiss (samples BDH 06, BDH 13B, BDH 16, BHD 3B, and BDH 77A): The rock comprises of Qtz, Kfs, Pl, Grt, Rt, Ms, Ilm, and Bt. Mnz, Ap, and Zrn occur as accessory phases. The rocks have a gneissic texture with alternating leucocratic (Qtz + Kfs + Pl) and Grt-rich layers. Leucocratic minerals show dynamic recrystallization, forming mylonitic foliation. Qtz underwent subgrain rotation and grain boundary migration, with cuspate Qtz-Kfs boundaries and thin films around Grt_2, indicating melt-present crystallization. Coarse xenoblastic Grt_2 contains inclusions of Qtz_1, Kfs_1, Bt_1, and Ilm_1. The augen gneiss consists of Qtz, Pl, Kfs, Grt, and Ilm along with Hbl and Bt. The rock shows dynamic recrystallization with mylonitic foliation defined by small recrystallized Qtz and feldspar grains, around feldspar porphyroclasts (up to 7 mm). The protomylonitic matrix has ribboned Qtz_2) with cuspate Kfs_2 grain boundaries. Porphyroblastic Grt_2 (up to 2 mm) contains flattened Qtz_1 inclusions.

LSD-2

Coarse-grained charnockite (samples BDH 62A and BDH 152): Rock shows granoblastic polygonal texture and relict igneous textures. Symplectite of Bt_3 and Qtz_3 partially replaces porphyroblastic Opx_2 and Grt_2 (Fig. 8h). Qtz_2, Kfs_2, and Pl_2 locally show cuspate mutual grain boundaries suggestive of melt-present crystallization.

Grt-Opx-bearing mafic granulite (samples BDH 34D and BDH 83C): The rock show an overall granoblastic texture of Grt_2, Opx_2, Pl_2, and Qtz_2 as the peak M_1 assemblage (Fig. 8i). Porphyroblastic Grt_2 grains contain inclusions of Qtz_1, Bt_1, Ilm_1, and Pl_1. The presence of fine cuspate Qtz grains surrounding Pl_1 indicates the former presence of the melt. The rock features a Grt corona (Grt_3) around Opx_2 and Ilm_2, separating them from Pl_2 (Fig. 8j). Cpx_3 is sometimes found with Grt_3 inside, while Qtz_3 forms intergrowths with Grt_3 on the outside.

Aluminous granulite (sample BDH 30 and BDH 34A): The rock is foliated with alternate Spl_2 + Sil_2 + Ilm_2 + Grt_2-rich and Qtz_2 + Pl_2 + Kfs_2-rich layers (Fig. 8k). The peak M_1 assemblage consists of coarse Grt_2, Spl_2, Sil_2 and Qtz_2. Coarse Grt_2 contains inclusions of Sil_1, Ilm_1, Qtz_1, and Bt_1. Sil_1 and Bt_1 are also present in Spl_2 (Fig. 8l). The occurrence of fine cuspate grains of Qtz surrounding Grt_2 indicates a former presence of the melt. A spongy intergrowth of Grt_3 + Qtz_3 surrounding porphyroblastic Grt_2. A double-layer corona of Sil_3, and Grt_3 separates Spl_2 from the matrix Qtz_2 developed during cooling after peak M_1 (Fig. 8m).

Calc-silicate granulite (sample BDH 62B): The rock has strong gneissic fabric with alternate thick melanocratic and leucocratic layers. The melanocratic layer contains a fine recrystallized aggregate of Cpx, Ttn, Qtz, Pl, and Cal. The leucocratic layers contain slightly coarser grains Cpx_2, wollastonite (Wo_2), Pl_2, Grt_2, Cal_2, and Qtz_2. Grt_3 forms a fine on Cpx_2 and Wo_2 to separate these minerals from Pl_2 (Fig. 8n). Grt_3 also forms fine intergrowth with Qtz_3 and such intergrowth locally replaces Cal_2 grains.

Orthopyroxene-bearing mafic granulite (sample BDH 28A): It is a massive rock that contains coarse Opx_2 forming granoblastic fabric with Pl_2, and Ilm_2. Both Opx_2 and Pl_2 show recrystallization with polygonal grain boundaries. Kfs_2 occurs occasionally as patchy antiperthite. Hbl_2 appears as patches on Opx_2 grains.

Host felsic gneiss (samples BDH 40 and BDH 17B): It shows a granoblastic polygonal texture where Grt_2 porphyroblasts are set in a quartzofeldspathic matrix. Relict igneous textures are preserved in Kfs_2 and Pl_2 grains.

8. WHOLE ROCK CHEMISTRY

Whole rock geochemistry has been done from the mafic enclave suites and host felsic gneiss from LSD-1 and LSD-2 and charnockite from LSD-2. Since the rocks have undergone high-grade metamorphism which has mobilized the major elements to leave the rock system, the REEs and trace elements have been used to characterize the geochemical evolution and tectonic affinities (Pearce, 1983).

Enclave suite of LSD-1 and LSD-2

The compositions of the mafic granulites, hornblendite, and hornblende gneisses encompasses the transition from andesite to basalt and beyond to picrobasalt sources when plotted in the TAS diagram (Middlemost, 1994). In the Nb_N-Th_N plot by Saccani (2015), all the mafic granulites plot in the MORB-OIB array (Fig. 9a). Hornblendite and hornblende gneiss samples plot in a continental arc setting (Hollocher et al., 2012). In the triangular diagram involving Th-Hf-Ta-Zr-Nb (Wood, 1980), all the samples plot within continental arc basalt (Fig. 9b).

Host felsic gneiss of LSD-1 and LSD-2

The felsic gneiss samples show composition from granite to granodiorite and belong to the ferroan group of granitoids when plotted in the SiO_2-Fe* diagram (Frost et al., 2001). They are peraluminous (ASI > 1.0) and show calcic to calc-alkalic affinity. Enrichment of Th and U indicates a crustal source. In the Hf-Rb-Ta diagram (Harris et al., 1986), all the samples plot within the volcanic arc setting, while the Zr/Y-Th/Yb plots (Ross & Bedard, 2009) suggest calc-alkaline affinity of the magmas (Fig. 9b).

Charnockites of the LSD-2

The two charnokite samples plot in the field of granodiorite to diorite and these show ferroan to magnesian characteristics in the SiO_2-Fe* plot (Frost et al., 2001). These are calcic to calc-alkalic and peraluminous (ASI > 1.0) in nature. Trace element and REE pattern show similarity with the felsic gneiss and the protolith magma having calc-alkaline affinity was emplaced in an arc setting (Yang et al., 2016, Hollocher et al., 2012).

9. GEOTHERMOBAROMETRY

LSD-1

The P-T conditions for the M_1 and M_{1R} metamorphic events were estimated using thermobarometry. M_1 prograde metamorphism of Grt + Cpx-bearing mafic granulites was calculated at 611–646°C and 5.4–6.5 kbar using the Grt_2-Hbl_1 assemblage. Peak M_1 conditions, based on Grt_2, Cpx_2, Qtz_2, and Pl_2 compositions, showed temperatures of 761–842°C at 12-14 kbar (Newton and Parkins, 1982; Moecher et al., 1988; Eckert et al., 1991). Core Grt_2 compositions indicated pressures of 11-14 kbar at 850°C, using models by Moecher et al. (1988) and Eckert et al. (1991).

The M_{1R} conditions were calculated using Grt_2 rim compositions with symplectic Cpx_3, Pl_3, and Opx_3. The Grt-Cpx thermometer (Ganguly, 1979) gave temperatures of 760–807°C at 8 kbar, while the grossular-anorthite-diopside-silica (GADS) barometer (Eckert et al., 1991) indicated pressures of 6.5-8 kbar at 750°C. The garnet-orthopyroxene-plagioclase-silica (GOPS) thermobarometer (Pattison et al., 2003) showed 604–622°C and 5.9-6.8 kbar. The Grt-Bt thermometer (Ganguly et al., 1996) gave 787–794°C, aligning with Ti-in-Bt thermometer (Henry et al., 2005) results of 754–775°C. P-T conditions of the M_2 metamorphism have been estimated by the Hbl-Pl thermobarometers (Holland and Blundy,

1994; Schmidt, 1992; Anderson and Smith, 1995) that yield temperature of 668–781°C, 4.7-7.6 kbar.

LSD-2

In Grt + Opx-bearing mafic granulite sample (BDH 34D), the Grt-Opx thermometer (Lee and Ganguly, 1988) gave temperatures of 735°C (core) and 696°C (rim) at 8 kbar. The grossular-anorthite-pyrope-enstatite-silica GAPES barometer (Eckert et al., 1991) yielded 7.3-7.6 kbar at 750°C, while the model of Pattison et al. (2003) gives lower estimates of 660°C/5.9 kbar and 542°C/5.2 kbar, respectively from the core and rim compositions. In sample BDH 83C, Grt-Opx thermometry gave 678–763°C, and Grt-Cpx thermometry (Ganguly, 1979) gave 732–793°C at 8 kbar. The maximum temperature was 850–863°C using Grt-Ilm thermometer (Pownceby et al., 1987). Pressures ranged from 5-8 kbar using various barometers at 750°C.

Two aluminous granulite samples were used to estimate peak metamorphic temperatures. Sample BDH 30 yielded 904–935°C, while BDH 34A gave slightly lower values of 895–912°C, both at 7.2 kbar using the Grt-Spl-Sil-Qtz thermometer (Nichols et al., 1992). Peak pressure was calculated at 7-7.4 kbar at 950°C using the Grt-Spl-Sil-Qtz barometer (Bohlen et al., 1986). Prograde temperatures were estimated between 600–782°C using the Ti in Bt thermometer (Henry et al., 2005), and retrograde temperatures ranged from 707–806°C based on matrix biotite analysis.

10. PHASE EQUILIBRIA ANALYSIS

The phase diagrams of mafic granulite samples from LSD-1 (Fig. 10a) show that the peak assemblage (Grt_2 + Cpx_2 + Pl_2 + Qtz_2 + Rt_2 + melt) is stable at pressures >8.5 kbar and temperatures >700°C, resulting from dehydration melting of Hbl-bearing assemblages. The stability field of the peak M_1 assemblage varies by sample ranges from >8.5-11.5 kbar and >680°-700°C. The residuum solidus occurs at ~700°C with a steep negative slope in all samples. The retrograde path of M_1 metamorphism (M_{1R}) for sample BDH 48 shows a pressure drop to 9 kbar at 800°C, with Hbl_3 appearing at 8 kbar and 750°C, indicating steep near-isothermal decompression (ΔP = 5.5 kbar). In BDH 3A, pressure decreases to 8 kbar (ΔP = 4 kbar) at 750°C, while in BDH 155D, decompression reaches 8.5 kbar (ΔP = 5 kbar) before Hbl_3 appears at lower P-T conditions. The pre-M1 assemblage in sample BDH 3A

includes Hbl_1, Pl_1, Ilm_1, and Qtz_1, stable below 7 kbar and 700°C. The $Hbl_2 + Cpx_2 + Grt_2 + Ilm_2 + Pl_2$ assemblage from the pre-M_1 stage is stable below 7 kbar and 730°C. In sample BDH 48, the same pre-M_1 assemblage is stable below 9 kbar and 750°C. The transition from pre-M_1 to peak M_1 and then to M_{1R} stages indicates a clockwise P-T trajectory.

Phase diagrams for the LSD-2 (Fig. 10b) were constructed for aluminous granulite sample BDH 30. The peak assemblage is stable in the temperature range of 960–1010°C and pressure range of 5.8-7 kbar from micro-bulk composition calculated from quantitative compositional mapping of the whole thin section area. The peak temperature (>960°C) may be slightly overestimated due to Zn in spinel. A median O_2 value of 0.2 wt.% was used for calculations, as the assemblage $Grt_2 + Kfs_2 + Spl_2 + Ilm_2 + Sil_2 + Qtz_2 + Pl_2$ + melt is stable at temperatures >800°C. The post-peak stage shows biotite appearance below 800°C, and the retrograde path indicates a pressure higher than 6.2 kbar, suggesting isobaric cooling down to ~650°C until melt crystallization. The prograde path remains undetermined, but peak and retrograde assemblages indicate a shallow dP/dT prograde stage in a counterclockwise P-T path typical of the EGP.

11. GEOCHRONOLOGY

Zircon U-Pb data:

LSD-1

Orthopyroxene granulite (sample BDH 155B): Low-CL cores show near-concordant (<5% discordance) dates in the range ca. 1075-1001 Ma (Th/U in the range 0.2-1.1). The interior part of the overgrowth domain or neoblastic zircon yields a $^{206}Pb/^{238}U$ mean age of 977 ± 12 Ma (n = 10, MSWD = 0.94). The peripheral part of the neoblastic zircon and overgrowth domain, as well as from the patchy cores yields a $^{206}Pb/^{238}U$ mean age of 904 ± 13 Ma (MSWD = 0.57) (Fig 11a).

Garnet-clinopyroxene mafic granulite (sample BDH 48): Inherited cores and low-CL cores show near-concordant spot dates in the range ca. 1039–1019 Ma (Th/U = 0.2-0.3). Moderate-CL cores of neoblastic zircon yields a $^{206}Pb/^{238}U$ mean age of 967 ±17 Ma (n = 8, MSWD = 1.4, Th/U = 0.2-0.4). The peripheral region of the neoblastic zircon and the overgrowth

domain, as well as the patchy cores, yield a $^{206}Pb/^{238}U$ mean age of 900 ± 13 Ma (n = 12, MSWD = 1.4, Th/U = 0.2-0.4) (Fig. 11b).

Garnet-clinopyroxene mafic granulite (sample BDH 3A): Th/U ratio from the featureless patchy domain varies widely (0.02-1.2) and the spot dates show variation in the range ca. 763-929 Ma, this population yields a 238U/206Pb mean age of 891 ± 23 Ma (n=5, MSWD=1.6). Some of the spots show reverse discordance. Data from the faintly oscillatory zoned domains show Th/U ratios in the range of 0.66-1.60 and the spot dates are nearly concordant in the range of ca. 917-988 Ma. These dataset yields a mean 238U/206Pb age of 956 ± 7 Ma (n=26, MSWD = 1.6) (Fig. 11c).

Hornblende gneiss (T69): Spots from the overgrowth and patchy domains yield slightly discordant (3.9% to -3.6%) data in the range ca. 707-823 Ma with variable Th/U ratio (0.14-1.01). Spots from the outer margin of the faint oscillatory-zoned domain are slightly discordant in the range ca. 837-911 Ma with a mean 238U/206Pb age of 885 ± 12 Ma (n=12, MSWD = 1.5). The Th/U ratio varies widely (0.28-2.30) for this domain. Spots from the interior part of the oscillatory-zoned zircon show slightly discordant data (4.7 to -4.5%), but a 238U/206Pb mean age of 939 ± 11 Ma (n=6, MSWD = 1.08) could be estimated. Th/U ratio varies within a narrow range (1.56-2.67) (Fig. 11d).

Felsic gneiss (sample BDH 06): Xenocrystic core yields a spot date of 1242 ± 29 Ma (Th/U = 0.4). Spots from the moderate-CL planar zoned neoblast and interior mantle yield a $^{206}Pb/^{238}U$ mean age of 964 ± 8 Ma (n = 17, MSWD = 1.5, Th/U = 0.3-0.6). The patchy interior of neoblasts, and unzoned exterior parts of the overgrowth domain show near-concordant age in the range of ca. 928-818 Ma showing a narrow Th/U ratio (0.3-0.4) (Fig. 11e).

Augen gneiss (sample BDH 3B): Oscillatory zoned domain yield a $^{206}Pb/^{238}U$ mean age of 959 ± 8 Ma (n = 19, MSWD = 1.3, Th/U = 0.1-1.4). Patchy zones and overgrowth domain yield a $^{206}Pb/^{238}U$ mean age of 914 ± 13 Ma (MSWD = 0.34, Th/U = 0.4-0.9) (Fig. 11f).

LSD-2

Hornblende granite (sample BDH 40): Oscillatory zoned domain yield a $^{206}Pb/^{238}U$ mean age of 947 ± 8 Ma (n=17, MSWD = 1.5, Th/U = 0.49-1.50). Patchy domain yields a $^{206}Pb/^{238}U$ mean age of 894 ± 19 Ma (n=7, MSWD = 1.8, Th/U = 0.49-1.50) (Fig. 11g).

Coarse-grained charnockite (sample BDH 62A): Oscillatory zoned domain yields a $^{206}Pb/^{238}U$ mean age of 978 ± 10 Ma (n=8, MSWD = 0.72, Th/U = 0.07-0.89). Featureless overgrowth and patches yield a $^{206}Pb/^{238}U$ mean age of 959 ± 6 Ma (n=20, MSWD = 1.11, (Th/U = 0.25-0.96) (Fig. 11h).

Monazite U-Th-total Pb data

LSD-2

Aluminous granulite (sample BDH 30, 34A): The central parts of matrix monazite and inclusions yield mean ages of 958 ± 15 Ma (n=12, MSWD=0.82) and 959 ± 8 Ma (n=33, MSWD=1.2). Patchy overgrowths show mean age of 899 ± 11 Ma (n=20, MSWD=0.43), 854 ± 18 Ma (n=6, MSWD=0.18), 797 ± 12 Ma (n=13, MSWD=1.11), and 653 ± 20 Ma (n=8, MSWD=1.4), with the youngest group averaging 535 ± 26 Ma (n=7, MSWD=1.8). The probability density plot shows a strong peak at ~959 Ma, followed by weak peaks ca. ~899 Ma, ca. 790 Ma, ca. 650 Ma, and ca. 530 Ma (Figs. 12a-b)

Felsic gneiss (sample BDH 08): The core region yields a mean age of 1012 ± 10 Ma (n=30, MSWD=0.49; Fig. 13a), while the mantle domain yields a spread of data in the range ca. 976-924 Ma with a mean age of 962 ± 9 Ma (n=31, MSWD=0.84; Fig. 13b). The overgrowth and outer patches show a wide range of spot dates varying from ca. 886 Ma to ca. 627 Ma.

Augen gneiss (sample BDH 03B): Spots from the core domain yield a mean age of 1010 ± 10 Ma (n=12, MSWD=0.94; Fig. 13c), while those from the mantle yields a data spread in the range ca. 970-919 Ma with a mean age of 952±5 Ma (n=68, MSWD=1.6; Fig. 13d). The spots from the overgrowth and patchy domain show a data range of ca. 896–652 Ma.

12. STRAIN, VORTICITY AND EBSD ANALYSES

3D-finite strain results obtained from feldspar porphyroclast shapes from eleven locations (Fig. 14a) show the result with low values √F between 0.4 and 8.8 %, indicating good elliptical adjustment and data quality (Table 3). The data show orientations of the XY plane of the strain ellipsoid to be E-W to WNW-ESE trending and dipping variably (35° to 80°) due N-NNE with poles (represented by the Z axes) gently to moderately plunging due S to SSW, which is very close to the average orientation of the mylonitic foliation as measured

from the MSZ outcrops (Fig. 14d). K-values (Flinn, 1962) measured from eleven sites across the MSZ suggest that for most sites the strain ellipsoid lies in the flattening field with values ranging from 0.18 to 0.73. However, for the sites L_4 and L_9, the measured K-values are 2.23 and 2.41, which indicates that the strain ellipsoid for these two sites lies in the constrictional field (Fig. 14c; Table 3). Calculated ν values (Hossack, 1968) for the samples similarly mostly lie in the flattening field (ν: 0.11 to 0.56; Fig. 14b; Table 3) excepting for the sites L_4 and L_9 (ν: -0.28 and -0.29; Fig. 14b; Table 3) that lie in the constrictional field. Finite strain data from feldspar clasts in augen gneiss suggests that deformation during S_{3MH} fabric formation in the MSZ varied from flattening to constriction ($\lambda 2 > 1$ to $\lambda 2 < 1$).

2D finite strain data were obtained from quartz grain shape measurements in XZ and YZ sections of three augen gneiss and one felsic gneiss mylonite samples (BDH 3B, BDH 14A, BDH 47, BDH 73) using the SPO method (Launeau and Robin, 2003). K and ν values vary from 0.07 to 0.67 and 0.15 to 0.83 respectively indicating strong flattening type deformation where $\lambda 2 > 1$ (Table 3; Figs. 14b, c) determined from S_{3ML} fabric.

Vorticity was measured from feldspar porphyroclasts in mylonitized augen gneiss at 13 locations across the MSZ using the PAR method (Passchier, 1987a; Wallis, 1995). The measured W_m values from thirteen sites across the width of the MSZ vary from 0.66 to 0.97 (Table 4) implying deformation under a simple shear regime.

EBSD analysis of quartz was performed from one mylonitic felsic gneiss sample (BDH 47) and two mylonitic augen gneiss samples (BDH 3B, BDH 14A) within the MSZ were analyzed. Pole figures from S_{3ML} fabric domains show two-point maxima near the Z direction of the c-axis, indicating consistent top-to-the-south reverse slip. This aligns with field and microstructural observations. CPO patterns suggest quartz deformation occurred by dislocation creep on basal <a> slip under low-to-medium grade conditions, with temperatures between 300°C and 500°C (Fig. 15).

13. DISCUSSION

Metamorphic evolution of the study area and time constraints

The textural, thermobarometric, and phase diagram modelling data suggest that the suite of mafic granulite enclaves within mylonitized felsic gneiss occurring along the WNW-ESE trending MSZ (LSD-1) preserves evidence of high-pressure metamorphism. The garnet-± clinopyroxene-bearing mafic granulite contains a mineral assemblage of garnet + clinopyroxene + plagioclase + quartz + rutile which was formed after dehydration melting of

hornblende-bearing protolith during an early (M_1) metamorphism peaked at 11-14 kbar, 760-840°C. The retrograde stage (M_{1R}) is marked by the formation of hornblende and symplectic intergrowth of clinopyroxene + plagioclase + orthopyroxene after garnet at 8-9 kbar, 760-810°C, suggesting an isothermal decompression type P-T path.

The rocks of the Phulbani domain (LSD-2) are represented by granulites with contrasting metamorphic characters. The garnet-±orthopyroxene-bearing mafic granulite within coarse-grained charnockite and the aluminous granulite enclave within felsic gneiss show evidence of biotite dehydration melting. The stable peak M_1 assemblage in the aluminous granulite is represented by the assemblage spinel + garnet + quartz + plagioclase + K-feldspar which was stable at 904–935°C, 7.0–7.4 kbar. The retrograde metamorphism (M_{1R}) in this rock is characterized by the reaction corona of garnet + sillimanite over spinel which formed at 700-738°C during near-isobaric cooling in an overall counterclockwise P-T path. The juxtaposition of lower crustal rocks showing clockwise and counterclockwise P-T paths across the MSZ as dismembered remnants of a paired metamorphic belt developed in a subduction-collision setting.

Zircon U-Pb and monazite U-Th-total Pb data from augen gneiss and enclave suite of rocks within the MSZ constrain peak M_1 metamorphism (D_{3MH} event) at ca. 980–960 Ma which was followed by decompression to a shallower level by ca. 960 Ma when the host granitic magma crystallized. The Phulbani domain, underwent UHT metamorphism at shallower crustal level broadly at the same time frame. A second metamorphic event (M_2) reworked the exhumed deep crustal rocks at ca. 900 Ma (Fig. 17). The weaker D_{3ML} greenschist facies occurred at a deformation temperature of 400°–500°C and lacked any zircon or monazite growth. Also, The ca. 535 Ma monazite data from aluminous granites of LSD-2 as well as earlier described K-Ar and Ar-Ar data from micas (ca. 504 Ma) of the MSZ (Crowe et al., 2001) indicate D_{3ML} event to be of Pan-African lineage (ca. 550–500Ma), related to fluid flow and shearing along reactivated shear system along the MSZ.

Kinematic interpretation

Systematic evaluation of shear sense criteria from XZ and YZ sections of the high-grade mylonitic fabric (S_{3MH}) domains (D_{3MH} event) reveal imprints of top-to-SW thrust sense and dextral strike slip displacements to be consistent in most samples. For the low-grade mylonitic fabric domains (S_{3ML}), however, only the top-to-SW thrust sense displacement in XZ sections is apparent (D_{3ML} event). Measured kinematic vorticity values representative of

the high-grade D_{3MH} and the low-grade D_{3ML} deformation events (Tables 3, 4; Figs. 16 a,b) point to the nature of deformation to be of sub-simple shear and simple shear type respectively. The nature of strain state during the high-grade D_{3MH} deformation has been shown to vary between flattening to constriction ($\lambda 2 > 1$ to $\lambda 2 < 1$) types in the MSZ rocks. In most sites across the MSZ, the strain value is high and varies from 2.59 to 5.50 with localized very high values of 15.24, 6.27 and 7.45 (Table 2; Fig. 14d) indicating heterogeneous strain intensity across the MSZ. In contrast, the Rxz values of the strain ellipsoid of the D_{3ML} deformation are comparatively less intense (from 1.56 to 2.40; Table 2, Figs. 14 b,c) and are dominantly of flattening type.

Combining structure, strain and vorticity data, a triclinic transpression model is considered to be most appropriate to generate the observed structures during the earlier granulite-facies shearing episode (D_{3MH}) along the MSZ (Fig. 18a). The D_{3MH} deformation was succeeded by the later upper greenschist-facies shearing event (D_{3ML}), for which the available data suggest a monoclinic transpressional deformation to be effective along the north- dipping MSZ (Fig. 18b). The present study indicates that the effect of the earlier high-grade deformation episode (D_{3MH}) is more pervasive as far as strain and fabric development is concerned within the MSZ rocks, while the second low-grade shearing event (D_{3ML}) left a weaker imprint suggesting the latter to be a phase of reworking along the MSZ.

The deformation kinematics in the MSZ footwall (Phulbani domain) is different from that of the MSZ proper. Though in the present study area or further south around Phulbani (Ganguly et al., 2021), the map-scale folds trend N to NNW, the general structural grain in northern EGP including the Phulbani domain is NE-SW (Dobmeier and Raith, 2003). The regional NE-SW trend rotates to N-NNW trend as the crustal-scale MSZ (present area) or RSZ (Ganguly et al., 2021) is approached. The NE-SW structural grain and the conjugate shear zones can be conceived to have formed under a protracted NW-SE compression in northern EGP in a pure shear-dominated deformation regime (Fig. 18a). The compression direction being lying in the NW quadrant, was oblique to the MSZ trend (Fig. 18a). The applied oblique compression was resolved in to length parallel dextral shearing and length normal compression plus reverse shear components in MSZ, with the rocks yielding under a protracted phase of triclinic transpression during the high-grade D_{3MH} event (Fig. 18a). During the later D_{3ML} event, the major compression direction must have changed to a new orientation nearly transverse to the MSZ trend resulting in the monoclinic transpression (Fig. 18b). The D_{3ML} event in this study thus should be considered as a phase of reworking along

the MSZ, possibly under the effects of the far field stresses of the Kuunga orogeny (Fig. 18b; Boger et al., 2002, 2011).

Tectonic Implications

Evidence of high pressure (11-14 kar, 760°–840°C) metamorphism (M_1) from a suite of mafic granulite enclaves indicates that the MSZ rocks suffered peak M_1 metamorphism at ca. 980-960 Ma, followed by a steep decompression (ΔP= 5.5 kbar; ΔT=70°C) path to shallower levels (8-9 kbar, ~700–750°C) by ca. 960 Ma, implying an uplift through thrusting of ~18 km of the thickened lower crust along a near-isothermal clockwise *P-T* path. Such a near-isothermal decompression-dominated clockwise *P-T* path is believed to authenticate collisional tectonics (Harley, 1989; England and Thompson, 1984) and imply presence of a ca. 970–900 Ma collisional history along the MSZ. It indicates that the former could represent a fossilized suture zone linked with possible terrane accretion and collision in northern EGP. It reinforces the suggestion earlier put forward by Banerjee et al. (2023), on the basis of discordance in metamorphic history-age data that the Angul domain represented an exotic terrane at ca. 1200 Ma, which was juxtaposed with the remaining EGP at or after ca. 960 Ma.

From presently generated structure, strain and vorticity data, a triclinic transpression model is considered to be most appropriate for the granulite-facies D_{3MH} shearing episode. Monazite data constrain the D_{3MH} event at ca. 950 – 900 Ma, which is presumed to be follow up of the high-P metamorphism (M_1; ca. 980–960 Ma) showing clockwise P-T path in the MSZ. The later D_{3ML} event occurred under upper greenschist facies conditions and left weaker impresses on the MSZ rocks. Available data suggest the D_{3ML} as a monoclinic transpressional event to be effective along the north- dipping MSZ. The present study exemplifies that the earlier high-grade deformation episode (D_{3MH}) is pervasive, while the second low-grade shearing event (D_{3ML}) left weaker impresses suggesting the latter to be a phase of reworking along the MSZ. Following Crowe et al. (2001), Ganguly et al. (2021) and Karmakar et al. (2024), the likely timing of the D_{3ML} event is placed at ca. 550–500 Ma.

In summary, present data demonstrate a long and complex evolutionary history for the collisional orogenic setting (D_{3MH} event) encompassing Phulbani-MSZ-Angul domains in the northern EGP, with ductile activity extending over ca. 80 Ma between 980 and 900 Ma (Ganguly et al., 2021; Banejee et al., 2023; Karmakar et al., 2024; present study). The D_{3MH} thrusting event at ca. 950–900 Ma along the MSZ is in conformity with the evidence of high

pressure rocks and clockwise P-T path in the MSZ (ca. 980-960 Ma; Karmakar et al., 2024) and together suggest for the development of a convergent setting in between the Phulbani and the Angul domains in the northern EGP during ca. 980-900 Ma. It resulted in convergence related subduction, high-*P* metamorphism of the subducting mafic rocks of the Phulbani domain, closure of the intervening ocean (Karmakar et al., 2024) followed by eventual oblique collision, docking and thrusting of the Angul domain atop the Phulbani domain along the N-NNE dipping MSZ. Overlapping timespan and overprinting relationships of the deformational-metamorphic episodes of the adjoining northern Angul, southern Phulbani and MSZ domains represent a tell-tale manifestation of this collisional process.

14. CONCLUSION

1. Evidence of high pressure (11-14 kbar, 760°–840°C) metamorphism (M_1) has been reported for the first time from a suite of mafic granulite enclaves present in host mylonitized felsic gneiss occurring along the E-W trending MSZ (LSD-1) which separates the Phulbani domain from the Angul-Tikarpara domain in the northern part of the EGP.

2. Geochronological data indicate that the enclave rocks suffered peak M_1 metamorphism at ca. 980-960 Ma, which was followed by a steep decompression (ΔP= 5.5 kbar; ΔT=70°C) path to shallower levels (8-9 kbar, ~700-750°C) by ca. 960 Ma. It implies an uplift through thrusting of ~18 km of the thickened lower crust along a near-isothermal clockwise P-T path along the MSZ. In contrast to the MSZ rocks, the southerly placed rocks of the Phulbani domain (LSD-2) underwent UHT metamorphism (anticlockwise P-T path) at shallower crustal levels broadly at the same time frame (ca. 960-970 Ma). Thus, the juxtaposition of lower crustal rocks showing clockwise and counterclockwise P-T paths across the MSZ implies the onset presence of a paired metamorphic belt in the Phulbani domain-Angul domain interface of the EGP indicating the occurrence of in a subduction-collision setting at ca. 960-970 Ma.

3. Systematic evaluation of shear sense criteria from XZ and YZ sections of the high grade mylonitic fabric (S_{3MH}) domains reveal imprints of top-to-SW thrust sense and dextral strike slip displacements to be consistent while for the low-grade mylonitic fabric domains (S_{3ML}), only the top-to-SW thrust sense displacement in XZ sections is apparent.

4. MSZ acted as an important terrane boundary juxtaposing India (Phulbani domain) and East Antarctica (Angul-Prydz Bay domain) during ~ 950–900 Ma. The mafic rocks of the MSZ bear the evidence of a fossilized suture zone of this terrane accretion and collision.

FUNDING and Acknowledgement

The author acknowledges financial support from CSIR-India through a research fellowship (File No.: 08/155 (0058)/2019-EMR-I).

REFERENCES

Abd El-Naby, H., Frisch, W. & Siebel, W., 2008. Tectono-metamorphic evolution of the Wadi Hafafit Culmination (central Eastern Desert, Egypt). Implication for Neoproterozoic core complex exhumation in NE Africa. Geologica Acta, 06, 293-312.

Alsop, G. I. & Holdsworth, R. E., 2006. Sheath folds as discriminators of bulk strain type. Journal of Structural Geology, 28, 1588-1606.

Anderson, J. L., & Smith, D. R., 1995. The effects of temperature and fO2 on the Al-in-hornblende barometer. American Mineralogist, 80, 549-559.

Banerjee, A., Ganguly, P., Sorcar, N., Das, K., & Bose, S., 2023. Contrasting styles of lower crustal metamorphism from a granulite suite of rocks from Angul, Eastern Ghats Belt, India: Implications for the India-Antarctica correlation. Journal of Petrology, https://doi.org/10.1093/petrology/egad065.

Bhadra, S., Gupta, S. & Banerjee, M., 2004. Structural evolution across the Eastern Ghats Mobile Belt- Bastar craton boundary, India: hot over cold thrusting in an ancient collision zone. Journal of Structural Geology, 26, 233-245.

Bhattacharya, A. & Gupta, S., 2001. A reappraisal of polymetamorphism in the Eastern Ghat Belt – A view from north of the Godavari rift. Journal of Earth System Science, 110, 369-383.

Bhowmik, S.K., 1997. Multiple episodes of tectonothermal processes in the Eastern Ghats granulite belt. Proceedings of Indian Academy of Science (Earth and Planetary Science), 106, 131– 146.

Bhowmik, S. K., Bose, S., Chattopadhyay, A., Karmakar, S., & Pant, N. C., 2024. Proterozoic mobile belts-magmatism, metamorphism, geochronology and tectonics in the context of formation of the Greater Indian Landmass. Proceedings of the Indian National Science Academy, 1-32.

Biswal, T. K., Waele, B. De & Ahuja, H., 2007. Timing and dynamics of the juxtaposition of Eastern Ghat Mobile Belt against the Bhandara Craton, India: A structural and zircon U-Pb SHRIMP study of the fold thrust belt and associated nepheline syenite plutons. Tectonics, 26 (4), TC4006.

Boger, S.D., 2011. Antarctica – before and after Gondwana. Gond. Res. 19, 335-371.

Boger, S.D., Wilson, C.J.L. & Fanning, C.M., 2001. Early Paleozoic tectonism within the East Antarctic craton: the final suture between east and west Gondwana?. Geology 29, 463–466.

Bohlen, S. R., Dollase, W. A., & Wall, V. J., 1986. Calibration and applications of spinel equilibria in the system FeO-Al2O3-SiO2. Journal of Petrology, 27, 1143-1156.

Bose. S., Fukuoka, M., Sengupta, P. & Dasgupta, S., 2000. Eolution of the high Mg-Al granulites from Sunkarametta, Eastern Ghats India: Evidence for a lower crustal heating-cooling trajectory. Journal of Metamorphic Geology, 18, 223-240.

Bose, S. & Das, K., 2006. Cordierite-K-Feldspar-Quartz Symplectite and its implication on the reworking of isobarically cooled crust: A case study from the Eastern Ghats Belt, India. Indian Journal of Geology, 78, 55-78.

Bose, S., Das, K., Dasgupta, S., Miura, H. & Fukuoka, M., 2006. Exsolution texture in orthopyroxene in aluminous granulites as indicators of UHT metamorphism: New evidence from the Eastern Ghats Belt, India. Lithos, 92, 506-523.

Bose, S., Das, K., Torimoto, J., Arima, M., & Dunkley, D. J., 2016. Evolution of the Chilka Lake granulite complex, northern Eastern Ghats Belt, India: First evidence of~ 780 Ma

decompression of the deep crust and its implication on the India–Antarctica correlation. Lithos, 263, 161-189.

Bose, S., Dunkley, D.J., Dasgupta, S., Das, K. & Arima, M., 2011. India-Antarctica-Australia-Laurentia connection in the Paleo-Mesoproterozoic revisited: Evidence from new zircon U-Pb and monazite chemical age data from the Eastern Ghats Belt, India. The Geological Society of America Bulletin, 123, 2031-2049.

Bose, S., Das, A., Samantaray, S., Banerjee, S. & Gupta, S., 2019. Late tectonic reorientation of lineaments and fabrics in the northern Eastern Ghats Province, India: Evaluating the role of the Mahanadi Shear Zone. Journal of Asian Earth Science. https://doi.org/10.1016/j.jseaes.2019.104071.

Bose, S. & Gupta, S., 2018. Strain partitioning along the Mahanadi Shear Zone: implications for paleo-tectonics of the Eastern Ghats Province, India. Journal of Asian Earth Sciences, 157, 269-282.

Bose, S. & Gupta, S., 2020. Evolution of stretching lineations in granulite-hosted ductile shear zones, Eastern Ghats Province, India: Role of temperature, strain rate and pre-existing stretching lineations. Journal of Structural Geology. https://doi.org/10.1016/j.jsg.2020.104127.

Bose, S., 2020. Geology of the Proterozoic Eastern Ghats Belt: Recent Developments and Outstanding Issues. Proc Indian Natn Sci Acad, 86, 87-97.

Bose, S., Sorcar, N., Das, K., Ganguly, P., & Mukherjee, S., 2022. Pulsed tectonic evolution in long-lived orogenic belts: an example from the Eastern Ghats Belt, India. Precambrian Research, 369, 106522. doi: 10.1016/j.precamres.2021.106522.

Cawood, P. A., Kröner, A., Collins, W. J., Kushy, T. M., Mooney, W. D. & Windley, B. F., 2009. Accretionary orogens through Earth history. Geological Society, London, Special Publications, 318, 1-36.

Chatterjee, A., Das, K., Bose, S. & Hidaka, H., 2017a. Age-integrated tectonic evolution across the orogeny-craton boundary: age zonation and shallow- to deep crustal participation during the Late Cambrian cratonisation of Eastern Ghats Belt, India. Lithos, 290-291, 269-293.

Chatterjee, A., Das, K., Bose, S., Ganguly, P. & Hidaka, H., 2017b. Zircon U-Pb SHRIMP and MONAZITE U-Th-total Pb geochronology of granulites of the western boundary, Eastern Ghats Belt, India: a new possibility for Neoproterozoic exhumation history. In: In: Dasgupta, S., Pant, N.C. (Eds.), Crustal Evolution of India and Antarctica: The Supercontinent Connection 457. Geological Society, London, Special Publications, 105-140.

Chetty, T. R. K., 2001. The Easterrn Ghats Mobile Belt, India: A collage of juxtaposed Terranes(?). Gondwana Research, 4, 319-328.

Chetty, T. R. K., 2010. Structural architecture of the Northern composite terrane, the Eastern Ghats Mobile Belt, India: Implications for Gondwana tectonics. Gondwana Research, 18, 565-582.

Chetty, T. R. K., 2014. Deep crustal shear zones in the Eastern Ghats Mobile Belt, India: Gondwana correlations. J. Ind. Geophys. Union, 18, 19-56.

Colliston, W. P., Praekelt, H. E. & Schoch, A. E., 1991. A progressive ductile shear model from the Proterozoic Aggeneys Terrane, Namaqua mobile belt, South Africa. Precambrian Research, 49, 205-215.

Crowe, W. A., Cosca, M. A., & Harris, L. B., 2001. 40Ar/39Ar geochronology and Neoproterozoic tectonics along the northern margin of the Eastern Ghats Belt in north Orissa, India. Precambrian Research, 108, 237-266.

Crowe, W. A., Nash, C. R., Harris, L. B., Leeming, P. M. & Rankin, L. R., 2003. The geology of the Rengali Province: implications for the tectonic development of the northern Orissa, India. Journal of Asian Earth Science, 21, 697-710.

Das, K., Bose, S., Ohnishi, I. & Dasgupta, S., 2006a. Garnet-spinel intergrowths in ultrahigh-temperature granulite, Eastern Ghats, India: Possible evidence of an Tschermak-rich orthopyroxene during prograde metamorphism. American Mineralogist, 91, 375-384.

Das, S., Nasipuri, P., Bhattacharya, A. & Swaminathan, S., 2008. The thrust contact between the Eastern Ghats Belt and the adjoining Bastar craton (Eastern india): Evidence from mafic granulites and tectonic implications. Precambrian Research, 162, 70-85.

Das, K., Bose, S., Karmakar, S., Dunkley, D. J. & Dasgupta, S., 2011. Multiple tectonometamorphic imprints in the lower crust: first evidence of ca. 950 Ma (zircon U-Pb

SHRIMP) compressional reworking of UHT aluminous granulites from the Eastern ghats Belt, India. Geol. J., 46, 217-239.

Das, K., Bose, S., Karmakar, S. & Chakraborty, S., 2012. Petrotectonic framework of granulites from northern part of Chilka lake area, Eastern Ghat belt, India: compressional vis-à-vis transpressional tectonics. Journal of Earth System Science, 121, 1-17.

Dasgupta, S., Bose, S. & Das, K., 2013. Tectonic evolution of the Eastern Ghats Belt. Precambrian Research, 227, 247-258.

Dasgupta, S., Sengupta, P., Ehl, J., Raith, M., & Bardhan, S., 1995. Reaction textures in a suite of spinel granulites from the Eastern Ghats Belt, India: evidence for polymetamorphism, a partial petrogenetic grid in the system KFMASH and the roles of ZnO and Fe2O3. Journal of Petrology, 36, 435-461.

Das, K., Bose, S. & Ghosh, G., 2017. The Neoarchean-Paleoproterozoic basin development and growth of the Singhbhum Craton, eastern India and its global implications: insights from detrital zircon U-Pb data. Precambrian Research, 298, 123-145.

Dasgupta, S., Bose, S., Bhowmick, S. K. & Sengupta, P., 2017. The Eastern Ghat Belt, India, in the context of supercontinent assembly. In: In: Dasgupta, S., Pant, N.C. (Eds.), Crustal evolution of India and Antarctica: The Supercontinent connection 457 Geological Society London Special Publications.

Dasgupta, S., 2020. Petrological evolution of the Eastern Ghat Belt- Current status and future directions. Journal of International Geoscience, 43, 124-131.

Dobmeier, J. C. & Raith, M.M., 2003. Crustal architecture and evolution of the Eastern Ghats Belt and adjacent regions of India. In (Yoshida, M., Windley, B.F., and Dasgupta, S., eds.) Proterozoic East Gondwana: Supercontinent Assembly and Breakup. Geological Society of London Special Publication 206, 145–168.

Eckert, J. O., Newton, R. C., & Kleppa, O. J., 1991. The ΔH of reaction and recalibration of garnet-pyroxene-plagioclase-quartz geobarometers in the CMAS system by solution calorimetry. American Mineralogist, 76, 148-160.

England, P. C., & Thompson, A. B., 1984. Pressure-temperature-time paths of regional metamorphism I. Heat transfer during the evolution of regions of thickened continental crust. Journal of Petrology, 25, 894-928.

Faleiros, M. F., Campanha, G. A. C., Martins, L., Vlach, S. R. F. & Vasconcelos, P. M., 2011. Ediacaran high-pressure collision metamorphism and tectonics of the Southern Ribeira Belt (SE Brazil): Evidence for terrane accretion and dispersion during Gondwana Assembly. Precambrian Research, 189, 263-291.

Faleiros, M, F., Campanha, G. A. C., Pavan, M., Almeida, V. V., Rodrigues, S. W. O. & Araújo, B. P., 2016. Short-lived polyphaser deformation during crustal thickening and exhumation of a collision orogen (Ribeira Belt, Brazil). Journal of Structural Geology, 93, 106-130.

Flinn, D., 1962. On folding during three-dimensional progressive deformation. Quarterly Journal of the Geological Society, 118(1-4), 385-428.

Frost, B. R., Barnes, C. G., Collins, W. J., Arculus, R. J., Ellis, D. J., & Frost, C. D., 2001. A geochemical classification for granitic rocks. Journal of Petrology, 42, 2033-2048.

Ganguly, P., Bose, S., Das, K., Torimito, J. & Ghosh, G., 2017. Origin of Spinel + Quartz Assemblage in a Si-undersaturated Ultrahigh-temperature Aluminous Granulite and its implications for the P-T-fluid History of the Phulbani Domain, Eastern Ghats Belt, India. Journal of Pterology, 58, 1941-1974.

Ganguly, P., Das, K., Bose, S., Ghosh, G., Hayasaka, Y. & Hidaka, H., 2018. U-Pb Zircon and U-Th-total Pb monazite ages from the Phulbani domain of the Eastern Ghats Belt, India: Time constraints on high-grade metamorphism and magmatism in the lower crust. Precambrian Research, 316, 1-23.

Ganguly, P., Ghosh, G., Bose, S., & Das, K., 2021. Polyphase deformation and ultrahigh temperature metamorphism of the deep continental crust: Implications for tectonic evolution of the northern Eastern Ghats Belt, India. Journal of Structural Geology, 143, 104250.

Ganguly, J., 1979. Garnet and clinopyroxene solid solutions, and geothermometry based on Fe-Mg distribution coefficient. Geochimica et Cosmochimica Acta, 43, 1021–1029.

Ganguly, J., Cheng, W., & Tirone, M., 1996. Thermodynamics of aluminosilicate garnet solid solution: new experimental data, an optimized model, and thermometric applications. Contributions to Mineralogy and Petrology, 126, 137-151.

Ghosh, A., Bhattacharyya, T., Kar, R. & Moharana, T., 2021. Structural framework of the transpressive Mahanadi Shear Zone and reevaluation of the regional geology in the northern sector of the Eastern Ghats Mobile Belt, Eastern India. International Journal of Earth Sciences, 110:1631-1652.

Ghosh, G., Bose, S., Mukhapadhyay, J. & Aich, S., 2010b. Remobilization of the southern margin of the Singhbhum craton, eatern India during the Eastern Ghats Orogeny. Indian Journal Geology, 80, 97-114.

Ghosh, G., Bose, S., Das, K., Dasgupta, A., Yamamoto, T., Hayasaka, Y., Chakrabarti, K. & Mukhopadhyay, J., 2016. Transpression and juxtaposition of middle crust over upper crust forming a crustal scale flower structure: Insight from structural, fabric, and kinematic studies from the Rengali Province, Eastern India. Journal of Structural Geology, 83, 156-179.

Henry, D. J., Guidotti, C. V., & Thomson, J. A., 2005. The Ti-saturation surface for low-to-medium pressure metapelitic biotites: Implications for geothermometry and Ti-substitution mechanisms. American Mineralogist, 90, 316-328.

Harley, S. L., 1989. The origins of granulites: a metamorphic perspective. Geological Magazine, 126, 215-247.

Holland, T., & Blundy, J., 1994. Non-ideal interactions in calcic amphiboles and their bearing on amphibole-plagioclase thermometry. Contributions to Mineralogy and Petrology, 116, 433-447.

Hollocher, K., Robinson, P., Walsh, E., & Roberts, D., 2012. Geochemistry of amphibolite-facies volcanics and gabbros of the Støren Nappe in extensions west and southwest of Trondheim, Western Gneiss Region, Norway: a key to correlations and paleotectonic settings. American Journal of Science, 312, 357-416.

Hossack, J.R., 1968. Pebble deformation and thrusting in the Bygdin area (southern Norway). Tectonophysics, 5(4), 315-339.

Janoušek, V., Farrow, C. M. & Erban, V., 2006. Interpretation of Whole-rock Geochemical Data in Igneous Geochemistry: Introducing Geochemical Data Toolkit (GCDkit). Journal of Petrology, 47, Issue 6, 1255–1259.

Katsube, A., Hyasaka, A., Sakaguchi, & Takahashi, Y., 2012. U-Pb zircon Dating Using Nd-YAG (213 nm) Laser Ablation-ICP-MS, and Evaluating the Consistency With SHRIMP Dating. Journal of the Geological Society of Japan, 118: 762-767 (in Japanese with English abstract).

Karmakar, S., Bose, S., Ghosh, G., Das, K., Sorcar, N. & Mukherjee, S., 2024. Evidence of High-Pressure Metamorphism along the Mahanadi Shear Zone in the Eastern Ghats Province, Eastern India: Implications on Tectonics and Continenetal Assembly Involving India and East Antarctica. Journal of Metamorphic Geology, https://doi.org/10.1111/jmg.12797.

Korhonen, F. J., Brown, M., Clark, C. & Bhattachraya, S., 2013a. Osumilite-melt interactions in ultrahigh temperature granulites: phase equilibria modelling and implications for the P-T-t evolution of the Eastern Ghats Province, India. Journal of Metamorphic Geology, 31, 881-907.

Kar, R., 2007. Dominal fabric development, associated microstructures and P-T records attesting to polymetamoprhism in a granulite complex of the Eastern Ghtas Granulites Belt, India. Journal of Earth System Science, 116, 21-35.

Korhonen, F. J., Clark, C., Brown, M., Bhattacharya, S. & Taylor, R., 2013b. How long-lived is ultrahigh temperature metamorphism? Constraints from zircon and monazite geochronology in the Eastern Ghats orogenic belt, India. Precambrian Research, 234, 322-350.

Lal, R. K., Ackermand, D. & Upadhyay, H., 1987. P–T –X relationships deduced from corona textures in sapphirine-spinel-quartz assemblages from Paderu, South India. Journal of Petrology, 28, 1139–1168.

Launeau, P., & Robin, P.-Y, 2003. SPO2003–Shape Preferred Orientation 2003. http://www.sciences.univ-nantes.fr/ geol/ SPO.

Law, R.D., 2010. Moine thrust zone mylonites at the Stack of Glencoul: II e results of vorticity analyses and their tectonic significance. In: Law, R.D., Butler, R.W.H., Holdsworth, R.E., Krabbendam, M., Strachan, R.A. (Eds.), Continental Tectonics and Mountain Building:

The Legacy of Peach and Horne. Geological Society, London, Special Publications, 335, 579e602.

Lee, H. Y., & Ganguly, J., 1988. Equilibrium compositions of coexisting garnet and orthopyroxene: experimental determinations in the system FeO-MgO-Al2O3-SiO2, and applications. Journal of Petrology, 29, 93-113.

Mahalik, N.K. 1994. Geology of the Contact between the Eastern Ghats Belt and North Orissa Craton, India. Journal of the Geological Society of India, 44 (1), pp. 41-51.

Mahapatra, S. N., Tripathy, A. K., Nanda, J. K. & Roy, A., 2009. Coexisting Ultramylonite and Pseudotachylyte from the Eastern Segment of the Mahanadi Shear zone, Eastern Ghats Mobile Belt. Journal Geological Society of India, 74, 679-689.

Middlemost, E. A., 1994. Naming materials in the magma/igneous rock system. Earth-Science Reviews, 37, 215-224.

Moecher, D. P., Essene, E. J., & Anovitz, L. M., 1988. Calculation and application of clinopyroxene-garnet-plagioclase-quartz geobarometers. Contributions to Mineralogy and Petrology, 100, 92-106.

Mondal, A. K., Bose, S., Sorcar, N., Tomson, J. K., Dev, J. A., & Mukherjee, S., 2023. Petrological, geochemical and geochronological evolution of massif type charnockite from the Eastern Ghats Province, India: implications on the regional tectonics of the Rayner-Eastern Ghats orogeny. Precambrian Research, 387, 106994.

Newton, R. C., & Perkins, D. III., (1982). Thermodynamic calibration of geobarometers based on the assemblages garnet-plagioclase-orthopyroxene (clinopyroxene)-quartz. American Mineralogist, 67, 203-222.

Nichols, G. T., Berry, R. F., & Green, D. H., 1992. Internally consistent gahnitic spinel-cordierite-garnet equilibria in the FMASHZn system: geothermobarometry and applications. Contributions to Mineralogy and Petrology, 111, 362-377.

Padmaja, J., Sarkar, T. & Dasgupta, S., 2024. Suturing of the Archean Bastar craton with the Eastern Ghats Province to from the Greater Indian Landmass: Insights from geochemistry, U-Pb geochronology and phase equilibria modelling. Precambrian Research, 412, 107536.

Padmaja, J., Sarkar, T., Dasgupta, S., Dash, J.K., Butani, R. & Chauhan, H., 2021. High pressure granulite facies metamorphism at the interface of the Archean Bastar craton and the Proterozoic Eastern Ghats Belt, India. Precambrian Research, 363, 106330.

Padmaja, J., Sarkar, T., Sorcar, N., Mukherjee, S., Das, N. & Dasgupta, S., 2022. Petrochronological evolution of Mg-Al granulites and associated metapelites from the contact zone of the Archean Bastar Craton and the Proterozoic Eastern Ghats Province, and its implications. Geosystems and Geoenvironment, 1, Issue 4, 100041.

Pal, S. and Bose, S., 1997. Mineral reactions and geothermobarometry in a suite of granulite facies rocks from Paderu, Eastern Ghats granulite belt: A reappraisal of the P-T trajectory. Proc. Indian Acad. Sci. (Earth Planet. Sci.), 106, 77-89.

Passchier, C.W., 1987a. Stable positions of rigid objects in non-coaxial flow—a study in vorticity analysis. Journal of Structural Geology, 9(5-6), 679-690.

Pattison, D. R., Chacko, T., Farquhar, J., & McFarlane, C. R., 2003. Temperatures of granulite-facies metamorphism: constraints from experimental phase equilibria and thermobarometry corrected for retrograde exchange. Journal of Petrology, 44, 867-900.

Pearce, J. A., 1983. Role of the sub-continental lithosphere in magma genesis at active continental margins. Continent Basalt and mantle xenoliths (pp. 230-249), Shiva Publication.

Pownceby, M. I., Wall, V. J., & O'Neill, H. St., 1987. Fe–Mn partitioning between garnet and ilmenite: Experiments and applications. Contributions to Mineralogy and Petrology, 97, 116–126.

Ramakrishnan, M., Nanda, J. K. and Augustin, P., 1998. Geological evolution of the Proterozoic Eastern Ghats Mobile Belt. In: Ramakrishnan, M., Paul, D. K. and Mishra, R. N. (Eds.) Geological Evolution of Proterozoic Eastern Ghats Mobile Belt. Geological Survey of India Special Publication, 44, 183-212.

Ranjan, S., Upadhyay, D., Abhinay, K., Pruseth, K. L. & Nanada, J. K., 2018. Zircon geochronology of deformed alkaline rocks along the Eastern Ghats Belt margin: India-Antarctica connection and the Enderbia continent. Precambrian Research. 310, 407-424.

Rickers, K., Mezger, K., & Raith, M. M., 2001. Evolution of the continental crust in the Proterozoic Eastern Ghats Belt, India and new constraints for Rodinia reconstruction: implications from Sm–Nd, Rb–Sr and Pb–Pb isotopes. Precambrian Research, 112, 183□210.

Saccani, E., 2015. A new method of discriminating different types of post-Archean ophiolitic basalts and their tectonic significance using Th-Nb and Ce-Dy-Yb systematics. Geoscience Frontiers, 6, 481-501.

Saha, D., Bhowmik, S. K., Bose, S. & Sanjeev, K., 2006. Proterozoic tectonics and Trans-Indian Mobile Belts: A status report. Proc. Indian Natn. Sci. Acad. 82, 445-460.

Saha, T. & Karmakar, S., 2015. Petrotectonic framework of the granitoids and associated granulites at the Nagavalli Shear Zone (NSZ), Eastern Ghats Belt: Evidence of a late transpression Orogeny. J. Earth Syst. Sci., 124, 707-727.

Sarkar, T., & Schenk, V., 2016. Early Mesoproterozoic (1.6–1.5 Ga) granulite facies events in the Ongole domain: geodynamic significance and global correlation. Journal of Metamorphic Geology, 34, 765-784.

Sarkar, M., Gupta, S. & Panigrahi, M. K., 2007. Disentangling tectonic cycles along a multiply deformed terrane margin: Structural and metamorphic evidence for mid-crustal reworking of the Angul granulite complex, Eastern Ghats Belt, India. Journal of Structural Geology, 29, 802-818.

Schmidt, M. W., 1992. Amphibole composition in tonalite as a function of pressure: an experimental calibration of the Al-in-hornblende barometer. Contributions to Mineralogy and Petrology, 110, 304-310.

Sengupta, P., Dasgupta, S., Bhattacharya, K. P., Fukuoka, M., Chakraborti, S. & Bhowmik, S., 1990. Petro-tectonic imprints in the sapphirine granulites from Anantagiri, Eastern Ghats Mobile Belt, India. Journal of Petrology, 31, 971–996.

Simmat R. and Raith, M. M., 2008. U-Th-Pb monazite geochronometry of the Eastern Ghats Belt, India: Timing and spatial disposition of poly-metamorphism. Precambrian Research, 162, 16-39.

Sorcar. N., Mukherjee, S., Pant, N.C., Dev, A. J. & N Nishanth., 2021. Chemical dating of monazite: Testing of analytical protocol for U–Th–total Pb using CAMECA SXFive tactis

EPMA at the National Centre for Earth Science Studies, Thiruvananthapuram, India. Journal of Earth System Science, 130, 234.

Strachan, R. A., Holdsworth, R. E., Krabbendam, M. & Alsop, G. I., 2010. The Moine Supergroup of NW Scotland: insights into the analysis of polyorogenic supracrustal sequences. Geological Society, London, Special Publications, 335, 233-254.

Upadhyay, D., Gerdes, A. & Raith, M. M., 2009. Unraveling Sedimentary Provenance and Tectonothermal history of High-Temperature Metapelites, Using Zircon and Monazite Chemistry: A case study from the Eastern Ghat Belt, India. The Journal of Geology, 117, 665-683.

Vadlamani, R., 2019. Cambrian Garnet Sm-Nd Isotopic Ages from the Ploydeformed Bolangir Anorthosite Complex, Esatern Ghats Belt, India: Implications for Intraplate Orogeny Coeval with Kuunga Orogenyduring Gondwana Assembly. The Journal of Geology, 127, 437-456.

Wallis, S., 1995. Vorticity analysis and recognition of ductile extension in the Sanbagawa belt, SW Japan. Journal of Structural Geology, 17(8), 1077-1093.

Wood, D. A. (1980). The application of a Th-Hf-Ta diagram to problems of tectonomagmatic classification and to establishing the nature of crustal contamination of basaltic lavas of the British Tertiary Volcanic Province. Earth and Planetary Science Letters, 50, 11-30.

Xypolias, P., 2009. Some new aspects of kinematic vorticity analysis in naturally deformed quartzites. Journal of Structural Geology, 31(1), 3-10.

Xypolias, P., Koukouvelas, I.K., 2001. Kinematic vorticity and strain rate patterns associated with ductile extrusion in the Chelmos Shear Zone (External Hellenides, Greece). Tectonophysics, 338, 59e77.

Yang, Q. Y., Santosh, M., Collins, A. S., & Teng, X. M. (2016). Microblock amalgamation in the North China Craton: evidence from Neoarchaean magmatic suite in the western margin of the Jiaoliao Block. Gondwana Research, 31, 96-123.

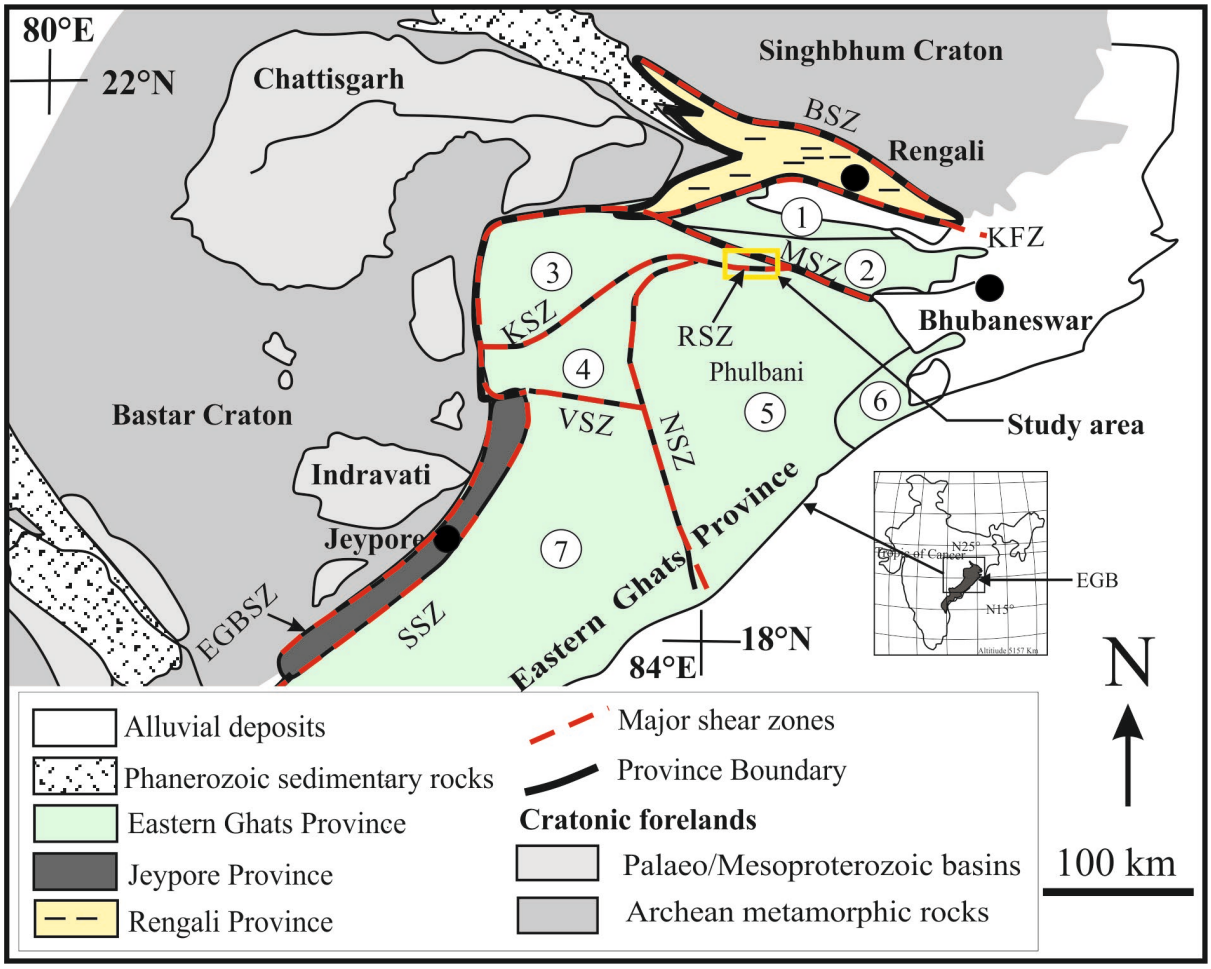

Figure 1: Geological map of the Eastern Ghats Belt showing the study area (marked by yellow-colored rectangle). The subdivisions of the crustal provinces into domains separated by megalineaments and shear zones are followed after Dobmeier & Raith (2003). Abbreviations used: BSZ: Barakot Shear Zone; EGBSZ: Eastern Ghats Boundary Shear Zone; KFZ: Kerajang Fault Zone; KSZ: Koraput Shear Zone; MSZ: Mahanadi Shear Zone; RSZ: Ranipathar Shear Zone; VSZ: Vamsadhara Shear Zone; NSZ: Nagavalli Shear Zone, SSZ: Sileru Shear Zone. The domains from north to south in the Eastern Ghats Province (EGP) are shown by encircled numbers: (1) Angul; (2) Tikarpara; (3) Khariar; (4) Rampur; (5) Phulbani; (6) Chilka; (7) Visakhapatnam.

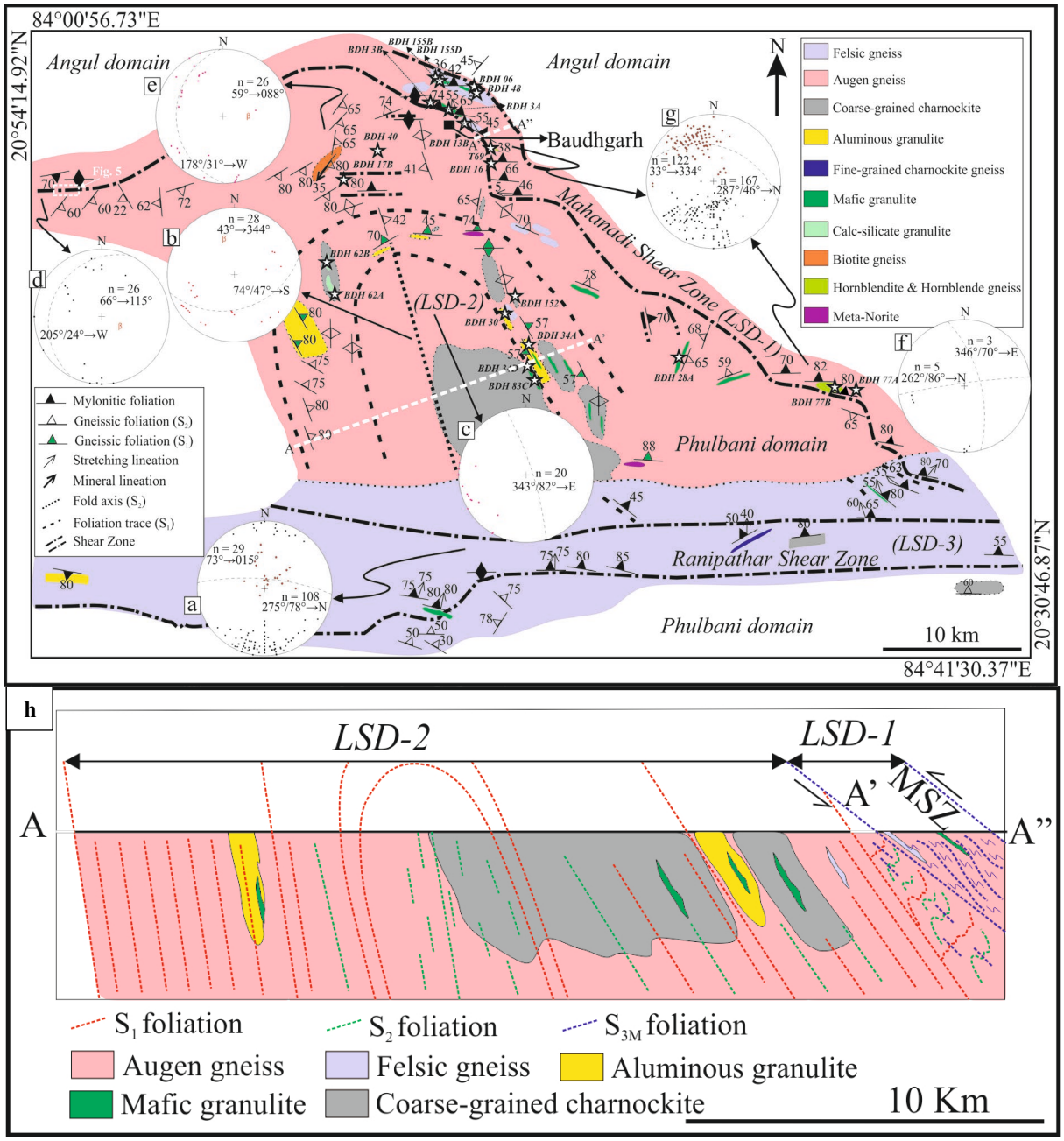

Figure 2: Geological map of the study area showing the disposition of the three Lithostructural domains (LSD 1-3). The locations of the representative sample from which petrological, geochemical and geochronological analyses were done are marked by 'star' marks. Structural data are shown in stereoplots (a-g). (h) Structural cross-section of the study area along the given line A-A'-A".

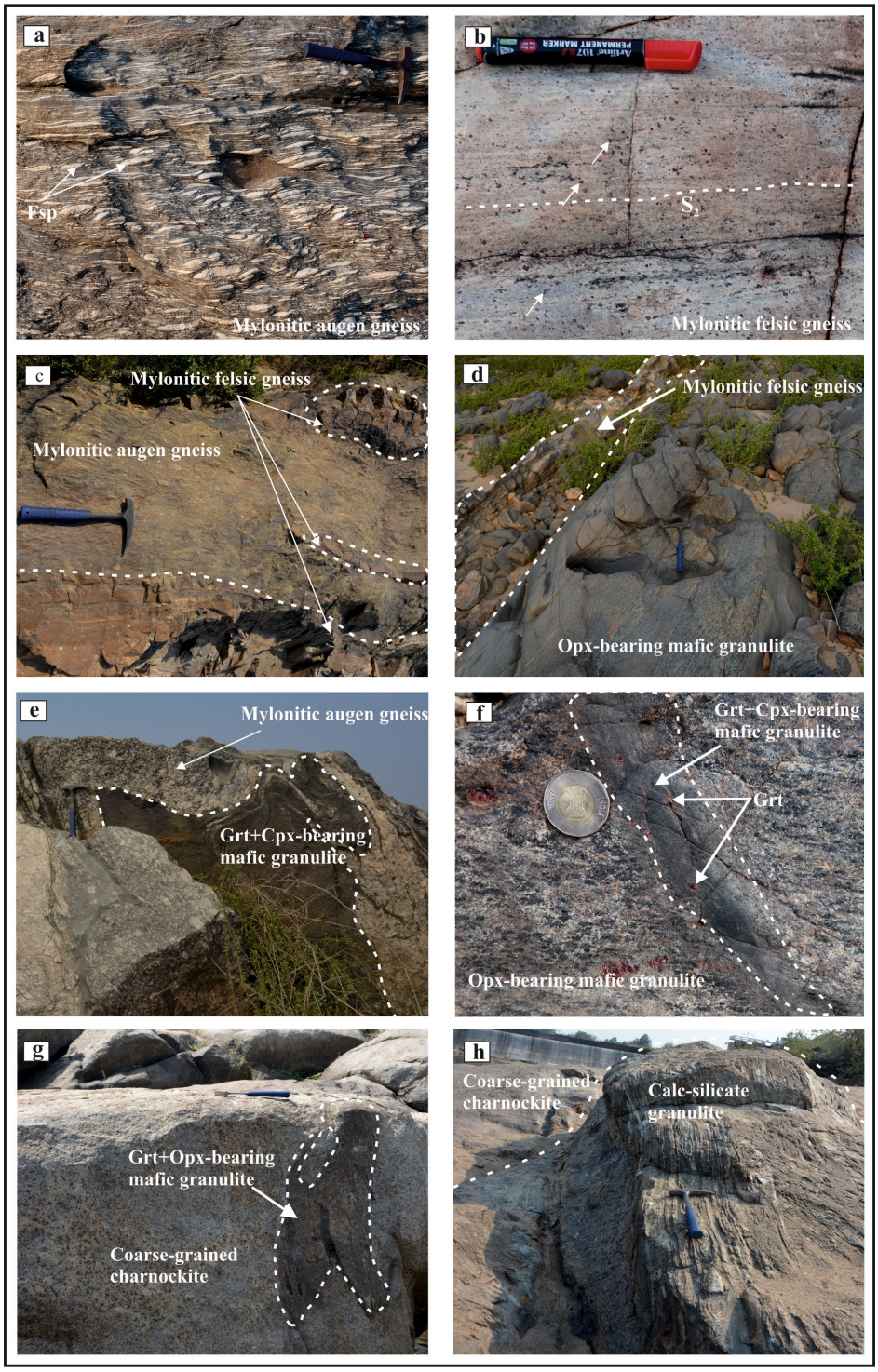

Figure 3: Field photographs of different lithologies and their relationships encountered within MSZ (LSD 1) (a-f) and in south of MSZ (LSD 2); (a) Mylonitic augen gneiss. (b) Mylonitic felsic gneiss (white dashed line indicating Grt + Bt-rich layer, while arrows indicating Grt grains). (c) Mylonitic felsic gneiss occurs as an enclave (indicated by a white dashed line) within mylonitic augen gneiss. (d) Opx-bearing mafic granulite occurring as an enclave within mylonitic felsic gneiss. (e-f) Grt + Cpx-bearing mafic granulite occurring as enclaves within mylonitic augen gneiss and Opx-bearing mafic granulite, respectively. Within LSD 2 (g-h); (g) Grt + Opx-bearing mafic granulite of LSD-2 occurring as an enclave within coarse-grained charnockite. (h) Calc-silicate granulite of LSD-2 occurs as an enclave within coarse-grained charnockite.

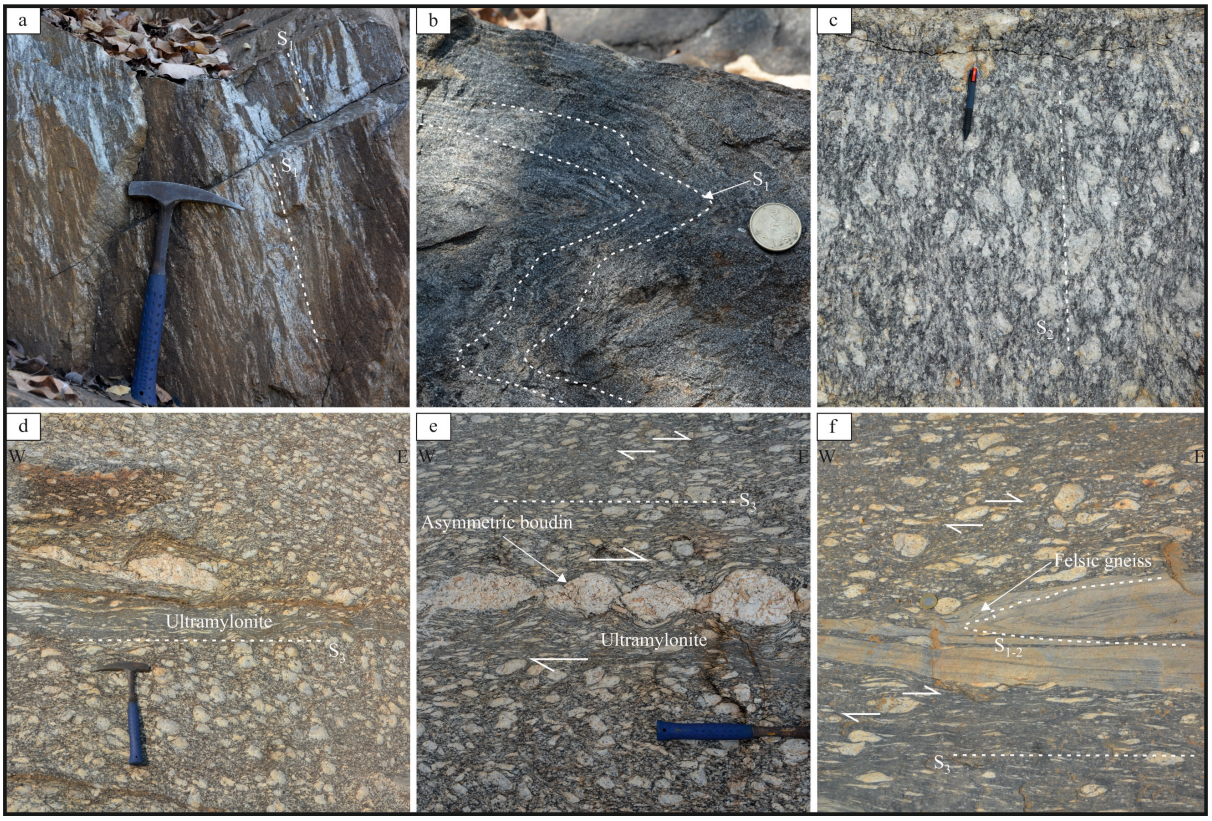

Figure 4: Field photographs showing important mesoscopic structural elements in LSD-2. (a) Aluminous granulite showing gneissic layering (S_1) marked by white-dashed line. (b) Mafic granulite with the S_1 gneissic layering folded to form F_2 folds. (c) Elongated porphyroclasts and biotite (Bt) grains within the porphyritic granite define the S_2 foliation. (d) Alternate mylonitic and ultramylonitic layers within porphyritic granite marking the S_3 foliation development in mesoscopic-scale shear zones. (e) Asymmetric boudin and feldspar augen with sigma-shaped tails showing dextral sense of shear on top surfaces of E-W trending mesoscopic-scale shear zones. (f) Enclaves of folded felsic gneiss within mylonitic porphyritic granite in E-W trending mesoscopic-scale shear zone.

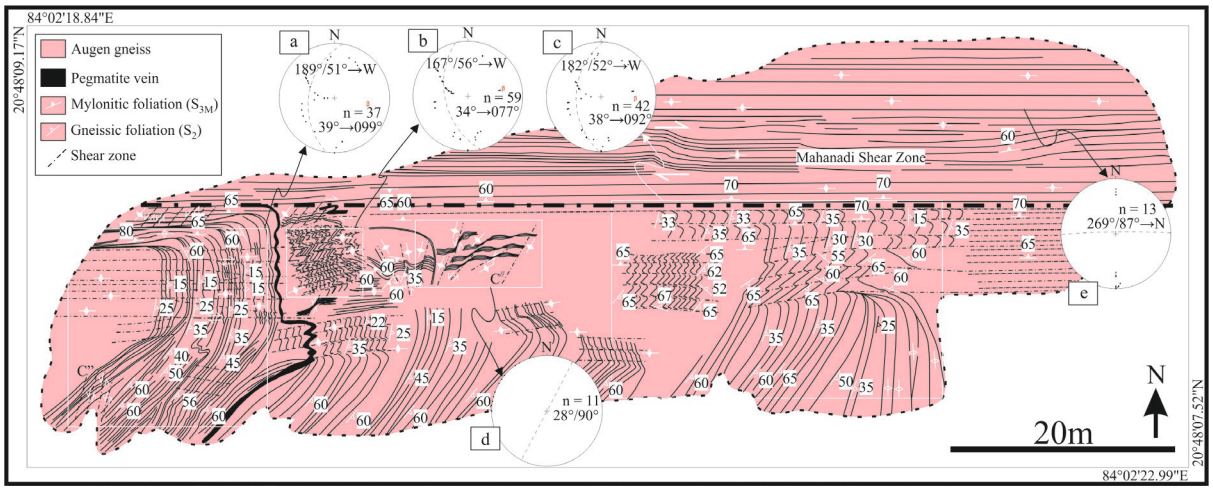

Figure 5: Large-scale structural map prepared from a part of the MSZ southern boundary (see Fig. 2 for location) illustrating the deformed S_2 foliation in augen gneiss and its transposition by S_{3M} mylonitic foliation. (a-c) Lower hemisphere equal area plots of poles to S_2 foliations showing development of asymmetric F_3 folds with varying orientations of fold axes (39°→099°, 34°→077°, 38°→092°); (d) Lower hemisphere equal area plot of poles to $C^{//}$ planes; (e) Lower hemisphere equal area plot of poles to S_{3M} mylonitic foliation (269°/87°N).

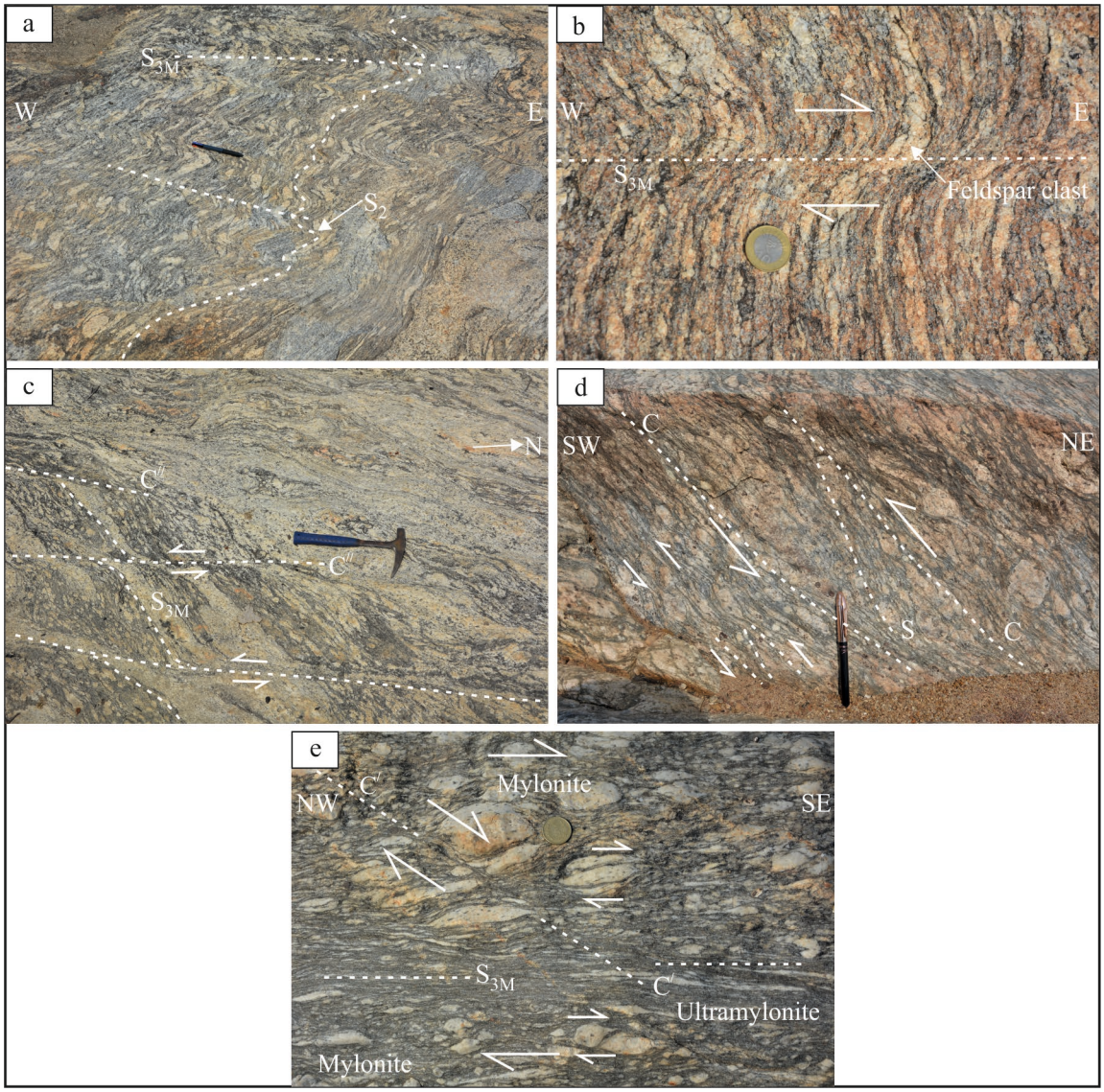

Figure 6: Field photographs showing important mesoscopic structural elements developed along the southern boundary of MSZ (a-c) and in the MSZ proper (d-e). (a) Asymmetric folds (F_3) developed on S_2 foliation within augen gneiss showing NE striking long southern limb, N-S trending, east-dipping hinge and E-W trending short northern limb. (b) Dextral sense of displacement along E-W trending S_{3M} mylonitic foliation on plan marked by deflection of S_2 layering. (c) NNE to NNW trending $C^{//}$ structures developed at high angle to the S_{3M} mylonitic foliation showing sinistral sense of shear. (d) S-C structures developed within mylonitic augen gneiss indicating top-to-the south reverse sense of shear on NE-SW trending vertical section. Note that recrystallized tails of feldspar clasts display a similar top-to-the south reverse sense of shear. (e) $C^{/}$ shear bands displace the C planes of S_{3M} mylonitic foliation (NW-SE trending) within augen gneiss showing consistent dextral slip displacement on the horizontal top surfaces of outcrops.

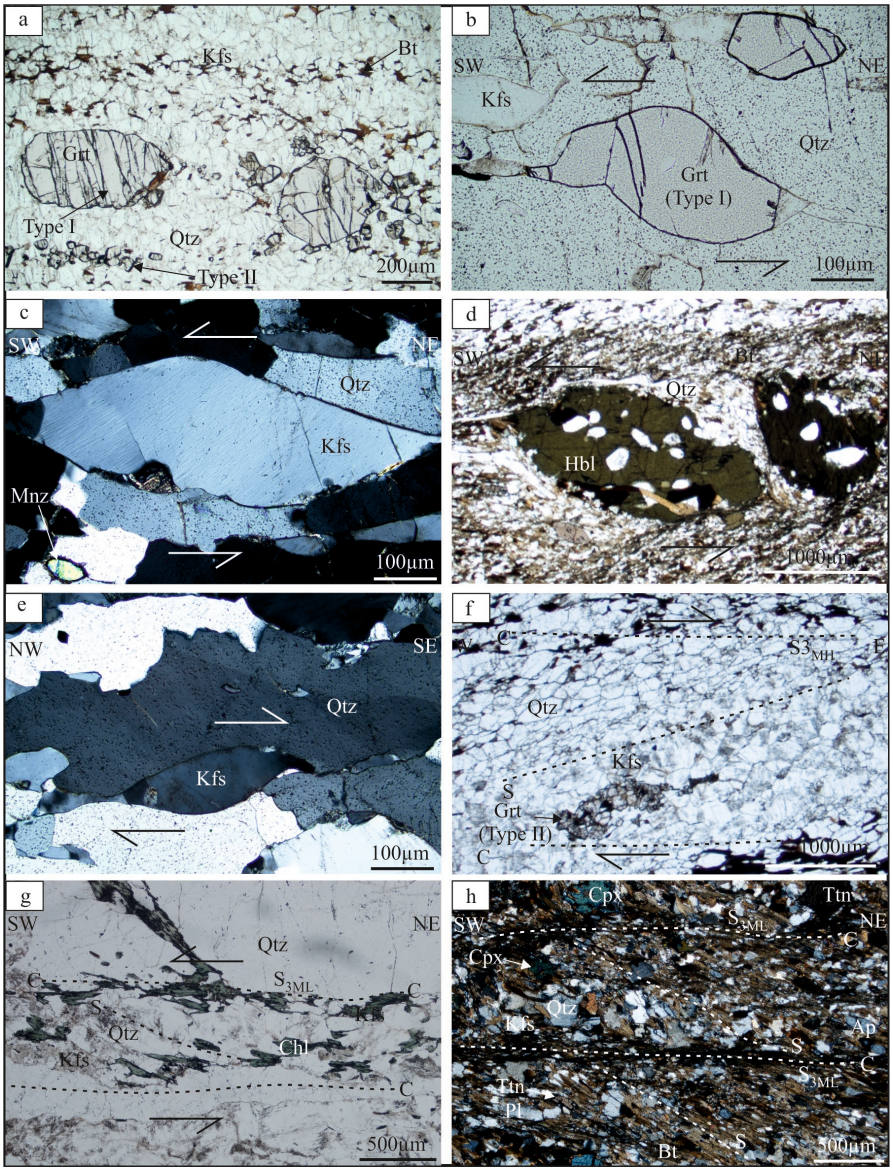

Figure 7: (a) Stretched garnet porphyroclast (Type I) and polycrystalline aggregates of garnet (Type II) occurring subparallel to stretched, recrystallized K-feldspar grains defining the S_{3MH} fabric in mylonitic augen gneiss; (b) Asymmetrically stretched garnet porphyroclast showing top-to-the SW reverse sense of shear in XZ section of mylonitic augen gneiss. (c) Asymmetrically stretched flame perthite grain with top-to-the SW reverse sense of shear in XZ sections of mylonitic augen gneiss; (d) Asymmetrically stretched hornblende grains in mafic granulite showing top-to-the SW reverse sense of shear; (e) Asymmetrically stretched K-feldspar grains in mylonitic felsic gneiss showing dextral sense of shear in sub-horizontal YZ sections; (f) S-C fabric in mylonitic augen gneiss defined by recrystallized quartz-feldspar and type II garnets indicating dextral sense of shear in sub-horizontal YZ sections. Photomicrographs of sheared MSZ rocks (LSD-1) from S_{3ML} fabric domains (g) Chlorite and recrystallized quartz-feldspar grains defining the S-C fabric within S_{3ML} fabric domains of mylonitic augen gneiss. The fabric asymmetry indicates top-to-the SW reverse sense of shear in XZ sections of the rocks; (h) S-C fabric defined by recrystallized quartz-feldspar and biotite grains in mafic granulite, the fabric asymmetry pointing to top-to-the SW reverse sense of shear in XZ sections of the rocks.

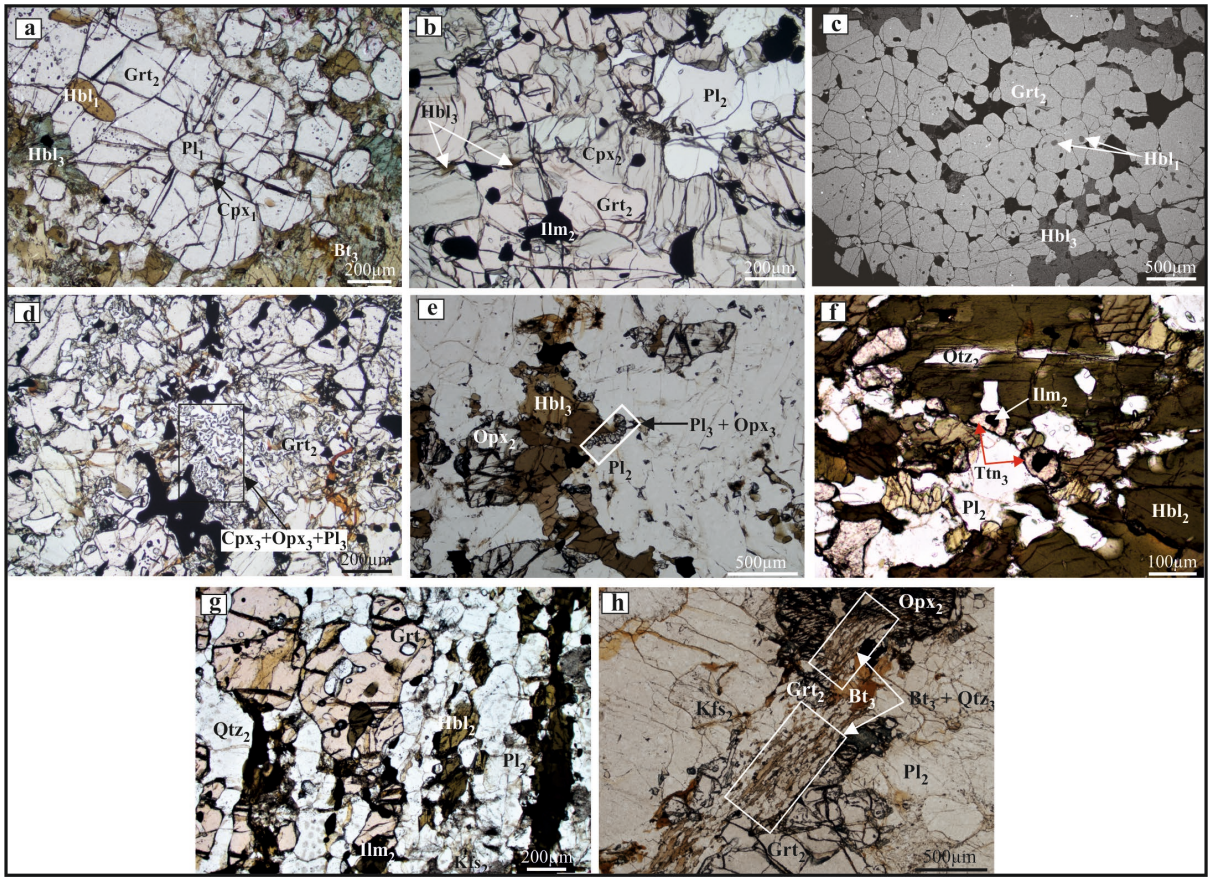

Figure 8: Textures and microstructures of mafic granulite enclaves of the LSD-1 and LSD-2. (a) Coarse garnet (Grt_2) grain with inclusions of hornblende (Hbl_1), clinopyroxene (Cpx_1) and plagioclase (Pl_1) surrounded by hornblende (Hbl_3) and biotite (Bt_3) in sample BDH 155D. (b) Granoblastic polygonal texture of garnet (Grt_2), clinopyroxene (Cpx_2), plagioclase (Pl_2) and ilmenite (Ilm_2) in sample BDH 48. Note the occurrence of hornblende (Hbl_3) as patches. (c) Backscatter electron (BSE) image of sample BDH 155D showing garnet (Grt_2) clusters with rounded inclusions of hornblende (Hbl_1). (d) Symplectic intergrowth of clinopyroxene (Cpx_3), orthopyroxene (Opx_3) and plagioclase (Pl_3) at the boundary of coarse garnet (Grt_2) in sample BDH 48. (e) Coarse Hbl_3 replacing Opx_2 along the foliation and showing breakdown to dusty intergrowth of Pl_3 and Opx_3 in sample BDH 155B. (f) Reaction corona of Ttn_3 surrounding Ilm_2 in sample BDH 77B. (g) Gneissic foliation shown by elongated hornblende (Hbl_2) and garnet (Grt_2) with alternate layers of plagioclase (Pl_2) and quartz (Qtz_2) in sample T 69. (h) Intergrowth of biotite and quartz (Bt_3 + Qtz_3) replacing garnet (Grt_2) and orthopyroxene (Opx_2) in sample BDH 62A.

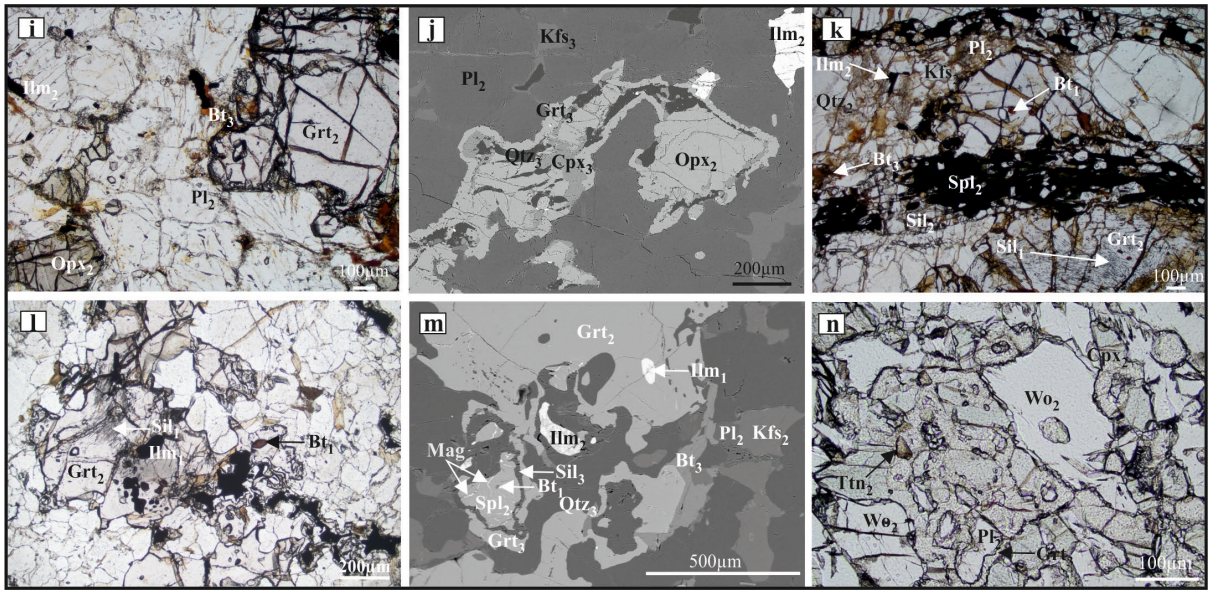

Figure 8: (i) Granoblastic texture of garnet (Grt_2), orthopyroxene (Opx_2), and plagioclase (Pl_2) in sample BDH 34D. Note the presence of tabular ilmenite (Ilm_2) and patchy biotite (Bt_3). (j) BSE image of sample BDH 83C showing thin garnet corona (Grt_3) along with clinopyroxene (Cpx_3) and quartz (Qtz_3) surrounding orthopyroxene (Opx_2) against coarse plagioclase (Pl_2). (k) Gneissic foliation shown by alternate melanocratic and leucocratic layers in sample BDH 30. The melanocratic layer is composed of spinel (Spl_2), garnet (Grt_2), sillimanite (Sil_2) and ilmenite (Ilm_2). The leucocratic layer is composed of quartz (Qtz_2), plagioclase (Pl_2) and K-feldspar (Kfs_2). (l) Coarse garnet (Grt_2) containing inclusions of fibrous sillimanite (Sil_1) and oval biotite (Bt_1) in sample BDH 30. (m) BSE image of sample BDH 30 showing double-layer corona of sillimanite (Sil_3) and garnet (Grt_3) on spinel (Spl_2). Exsolved magnetite (Mag) occurring in Spl_2 which also includes rounded biotite (Bt_1). (n) Photomicrograph showing presence of thin garnet (Grt_3) corona separating clinopyroxene (Cpx_2) and wollastonite (Wo_2) from plagioclase (Pl_2) in sample BDH 62B.

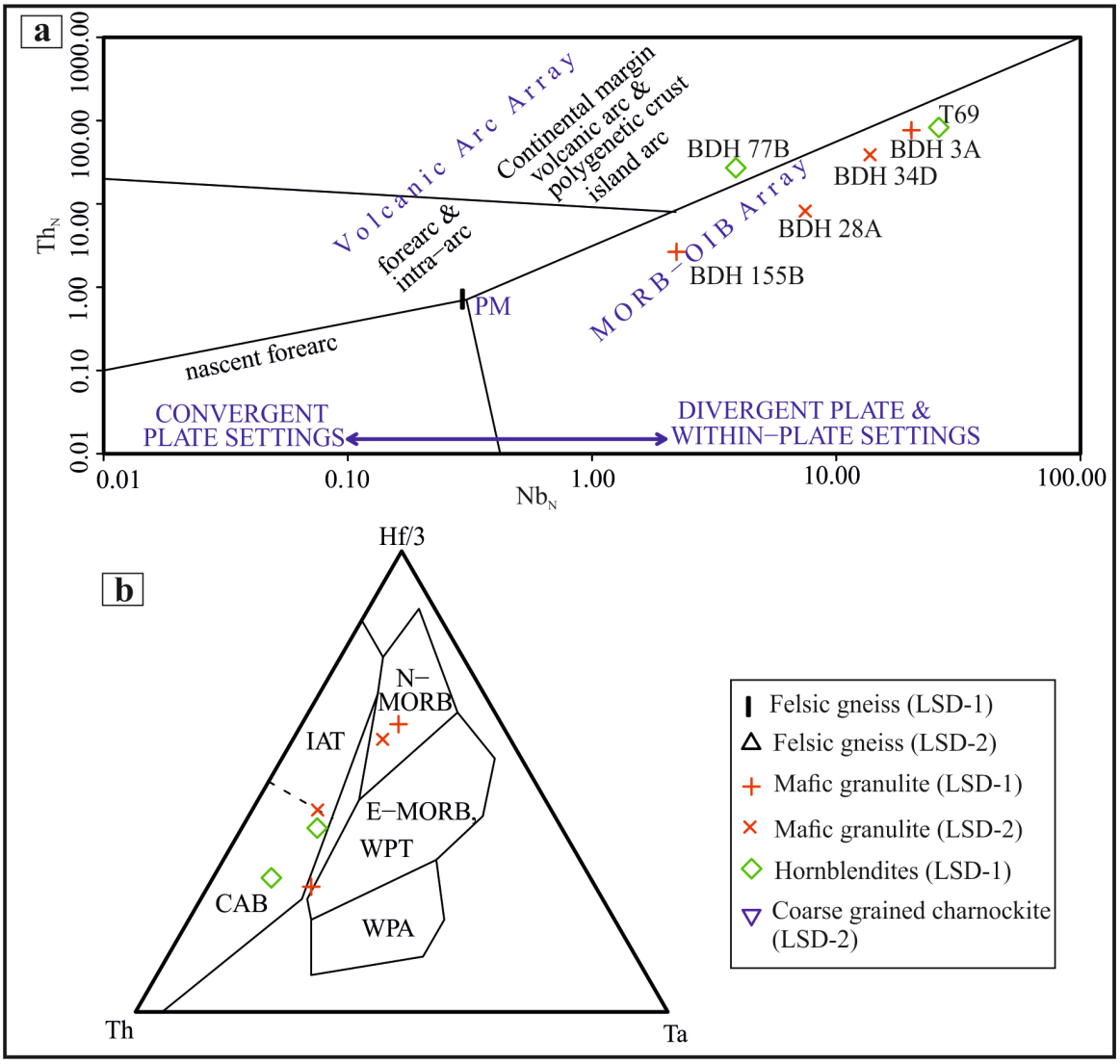

Figure 9: Plots of geochemical data from representative samples of LSD-1 and LSD-2. (a) Nb_N-Th_N plot (Saccani, 2015); (b) Th-Hf-Ta triangular plot (Wood, 1980).

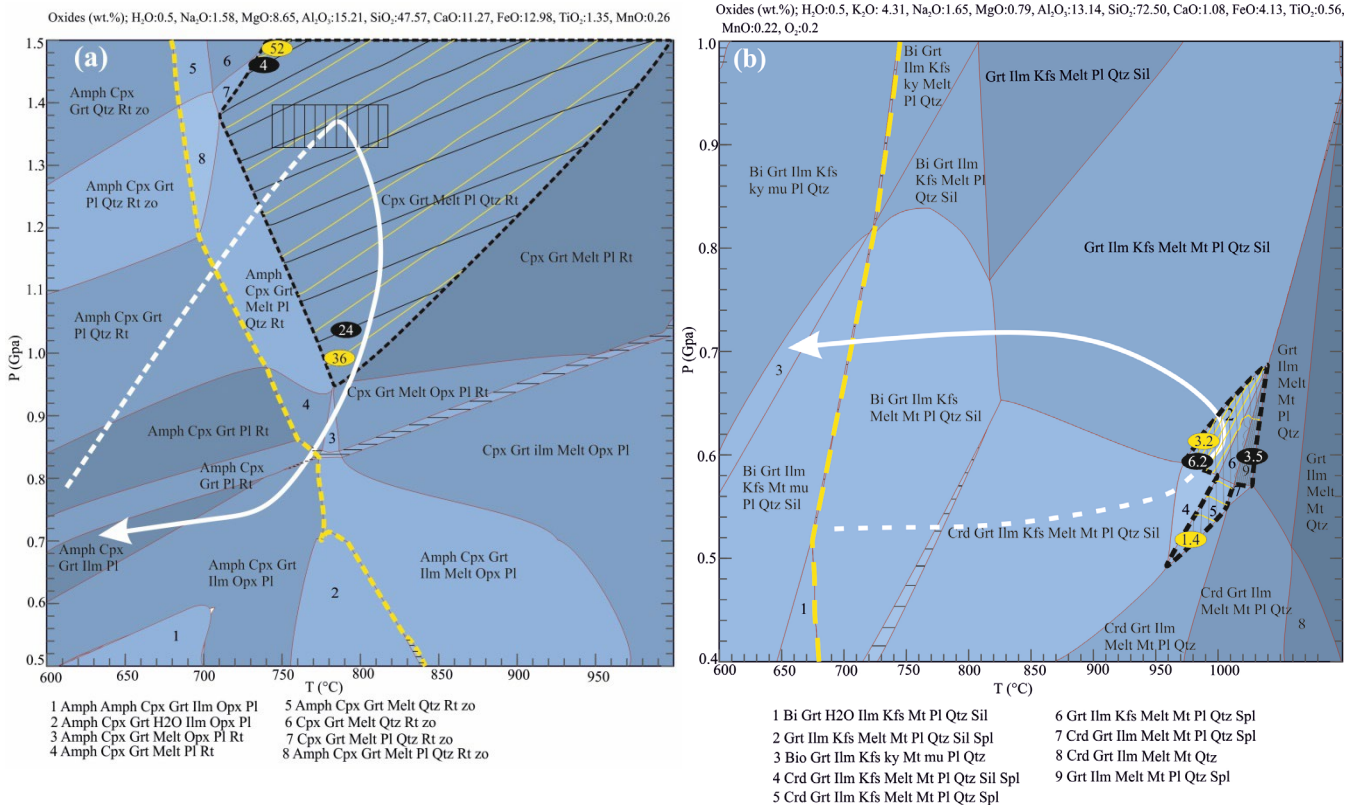
Oxides (wt.%); H2O:0.5, Na2O:1.58, MgO:8.65, Al2O3:15.21, SiO2:47.57, CaO:11.27, FeO:12.98, TiO2:1.35, MnO:0.26
(a)
Amph Cpx Grt Qtz Rt zo
Amph Cpx Grt Pl Qtz Rt zo
Cpx Grt Melt Pl Qtz Rt
Cpx Grt Melt Pl Rt
Amph Cpx Grt Melt Pl Qtz Rt
Amph Cpx Grt Pl Qtz Rt
Cpx Grt Melt Opx Pl Rt
Amph Cpx Grt Pl Rt
Cpx Grt ilm Melt Opx Pl
Amph Cpx Grt Pl Rt
Amph Cpx Grt Ilm Pl
Amph Cpx Grt Ilm Opx Pl
Amph Cpx Grt Ilm Melt Opx Pl
P (Gpa)
T (°C)
1 Amph Amph Cpx Grt Ilm Opx Pl
2 Amph Cpx Grt H2O Ilm Opx Pl
3 Amph Cpx Grt Melt Opx Pl Rt
4 Amph Cpx Grt Melt Pl Rt
5 Amph Cpx Grt Melt Qtz Rt zo
6 Cpx Grt Melt Qtz Rt zo
7 Cpx Grt Melt Pl Qtz Rt zo
8 Amph Cpx Grt Melt Pl Qtz Rt zo
Oxides (wt.%); H2O:0.5, K2O: 4.31, Na2O:1.65, MgO:0.79, Al2O3:13.14, SiO2:72.50, CaO:1.08, FeO:4.13, TiO2:0.56, MnO:0.22, O2:0.2
(b)
Bi Grt Ilm Kfs ky Melt Pl Qtz
Grt Ilm Kfs Melt Pl Qtz Sil
Bi Grt Ilm Kfs ky mu Pl Qtz
Bi Grt Ilm Kfs Melt Pl Qtz Sil
Grt Ilm Kfs Melt Mt Pl Qtz Sil
Bi Grt Ilm Kfs Melt Mt Pl Qtz Sil
Grt Ilm Melt Mt Pl Qtz
Bi Grt Ilm Kfs Mt mu Pl Qtz Sil
Crd Grt Ilm Kfs Melt Mt Pl Qtz Sil
Grt Ilm Melt Mt Qtz
Crd Grt Ilm Melt Mt Pl Qtz
Crd Grt Ilm Melt Mt Pl Qtz
P (Gpa)
T (°C)
1 Bi Grt H2O Ilm Kfs Mt Pl Qtz Sil
2 Grt Ilm Kfs Melt Mt Pl Qtz Sil Spl
3 Bio Grt Ilm Kfs ky Mt mu Pl Qtz
4 Crd Grt Ilm Kfs Melt Mt Pl Qtz Sil Spl
5 Crd Grt Ilm Kfs Melt Mt Pl Qtz Spl
6 Grt Ilm Kfs Melt Mt Pl Qtz Spl
7 Crd Grt Ilm Melt Mt Pl Qtz Spl
8 Crd Grt Ilm Melt Mt Qtz
9 Grt Ilm Melt Mt Pl Qtz Spl

Figure 10: Phase diagrams for representative samples of LSD-1 (a) and LSD-2 (b). (a) Phase diagrams of the sample BDH 48, respectively in the system Na_2O-CaO-FeO-MnO-MgO-Al_2O_3-SiO_2-TiO_2-H_2O. Bulk composition for each sample was calculated from XRF data as given in each diagram. The three diagrams show that the peak M_1 granulite assemblage of Grt-Cpx-Pl-Qtz has been derived from Hbl-bearing assemblage through a steep *dP*/*dT* prograde path reaching maximum *P* of 1.2-1.4 GPa. The peak position has been bracketed by the disposition of modal isopleth of Grt (yellow lines) and plagioclase (black lines). The intersections of isopleths show the *P*-*T* range of the peak condition for each sample. The diagrams also show the lower *P*-*T* margin of the peak assemblage in each sample (shown by dashed line). The position of melt-in line is shown in each diagram (stippled black line). Based on the textures and calculated isopleth values, the retrograde *P*-*T* path in each sample is shown. The overall *P*-*T* path is clockwise with steep compression during prograde stage and decompression during retrograde stage. (b) Phase diagram of the aluminous granulite sample BDH 30 from the LSD-2 in the system K_2O-Na_2O-CaO-FeO-MnO-MgO-Al_2O_3-SiO_2-TiO_2-H_2O. The bulk composition shown in the diagram has been calculated using chemical mapping of the whole thin section (see text for details). The peak M_1 metamorphic assemblage Grt-Spl-Sil-Qtz (marked by spaced dotted black line) shows a nearly shallow *dP/dT* curve followed by a near-isobaric cooling indicates a counterclockwise *P*-*T* path. The position of the melt-in curve is also shown (stippled black line).

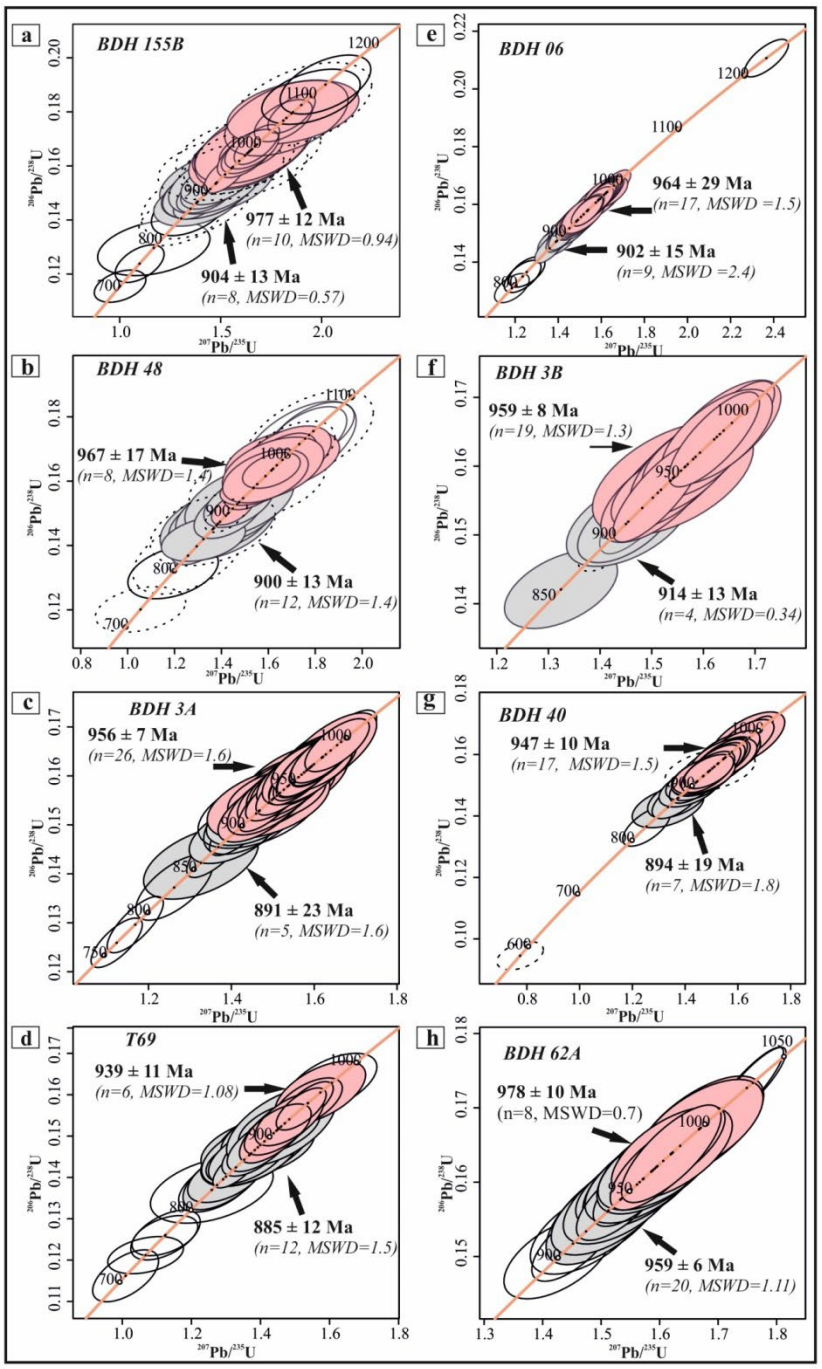

Figure 11: Wetherill concordia plots of analyzed zircon grains from the representative samples of LSD-1 (a-f) and LSD-2 (g-h) with $^{206}Pb/^{238}U$ weighted mean ages from different groups (see text). Spot dates shown as bold black ellipses were not considered for group age calculation due to high error or higher discordance (>5%). (a) Sample BDH 155B, (b) sample BDH 48, (c) sample BDH 3A, (d) sample T 69, (e) sample BDH 06, (f) sample BDH 3B, (g) sample BDH 40 and (h) sample BDH 62A.

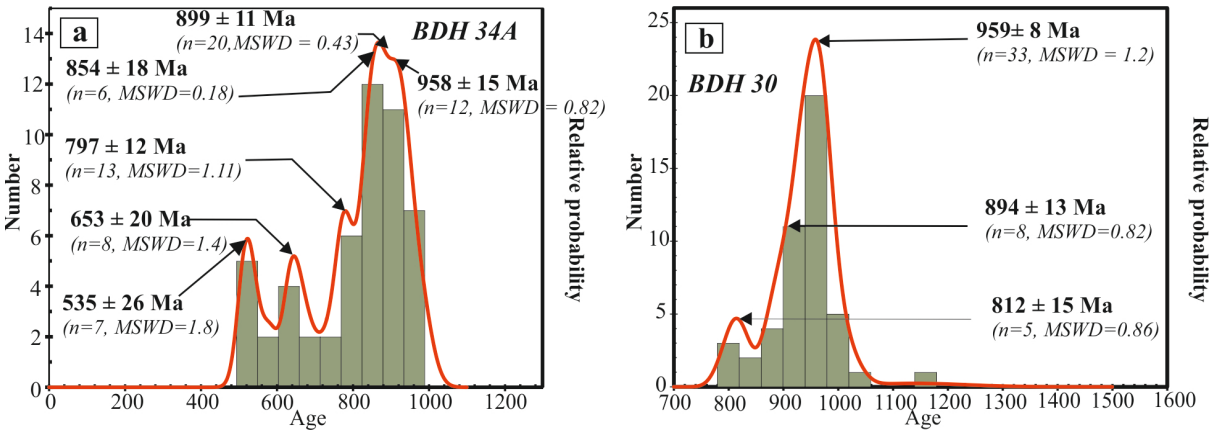

Figure 12: Textures and ages of representative monazite grains in aluminous granulite samples (BDH 34A and BDH 30) of LSD-2. (a) Probability density plot of all the analyzed monazite data of sample BDH 34A showing prominent age peaks as calculated from weighted mean ages. (b) Probability density plot of all the analyzed monazite data of sample BDH 30 showing prominent age peaks as calculated from weighted mean ages.

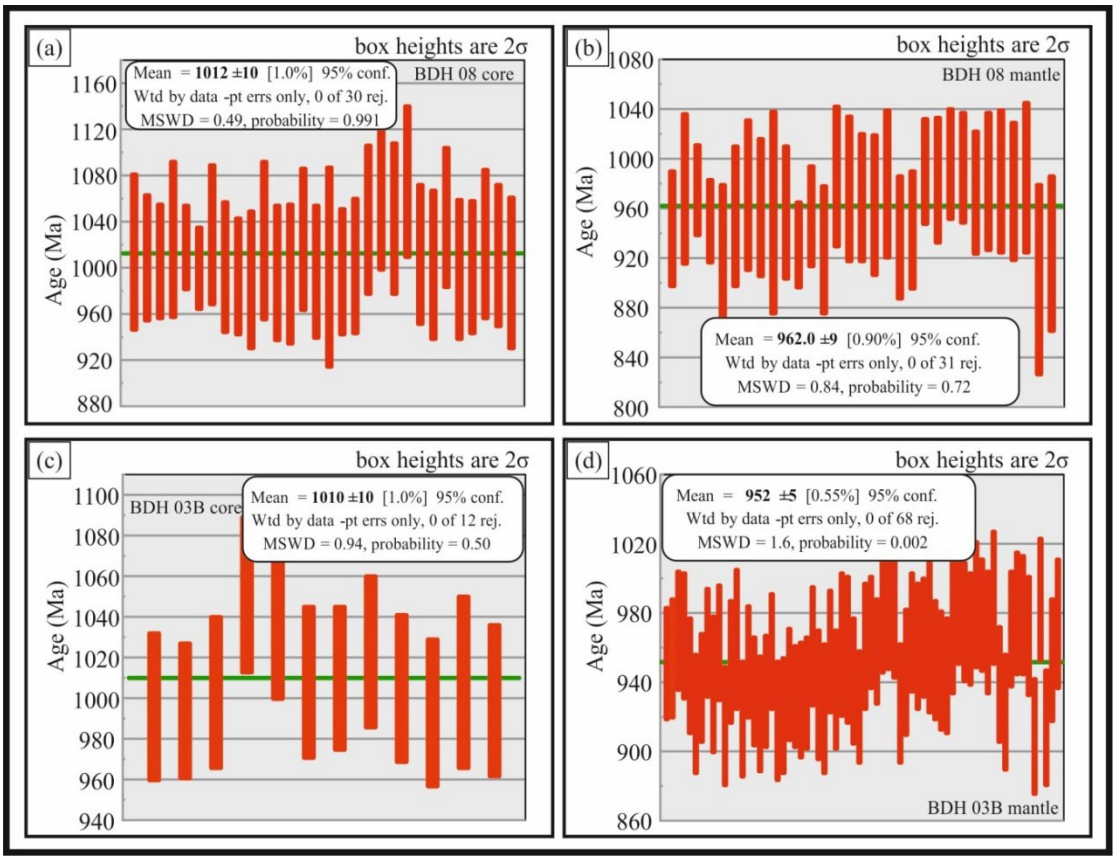
(a)
box heights are 2σ
Mean = 1012 ±10 [1.0%] 95% conf.
Wtd by data -pt errs only, 0 of 30 rej.
MSWD = 0.49, probability = 0.991
BDH 08 core
Age (Ma)
(b)
box heights are 2σ
BDH 08 mantle
Mean = 962.0 ±9 [0.90%] 95% conf.
Wtd by data -pt errs only, 0 of 31 rej.
MSWD = 0.84, probability = 0.72
Age (Ma)
(c)
box heights are 2σ
BDH 03B core
Mean = 1010 ±10 [1.0%] 95% conf.
Wtd by data -pt errs only, 0 of 12 rej.
MSWD = 0.94, probability = 0.50
Age (Ma)
(d)
box heights are 2σ
Mean = 952 ±5 [0.55%] 95% conf.
Wtd by data -pt errs only, 0 of 68 rej.
MSWD = 1.6, probability = 0.002
BDH 03B mantle
Age (Ma)

Figure 13: (a) Weighted average age of 1012 ± 10 Ma calculated from the spot data of core region from included monazite, partially included and matrix monazite. (b) Weighted average age of 962 ± 9 Ma calculated from the spot data of mantle domain of included monazite, partially included and matrix monazite. (c) Weighted average age of 1010 ± 10 Ma calculated from the spot data of core region from matrix monazite. (d) Weighted average age of 952 ± 5 Ma calculated from the spot data of mantle domain of matrix monazite.

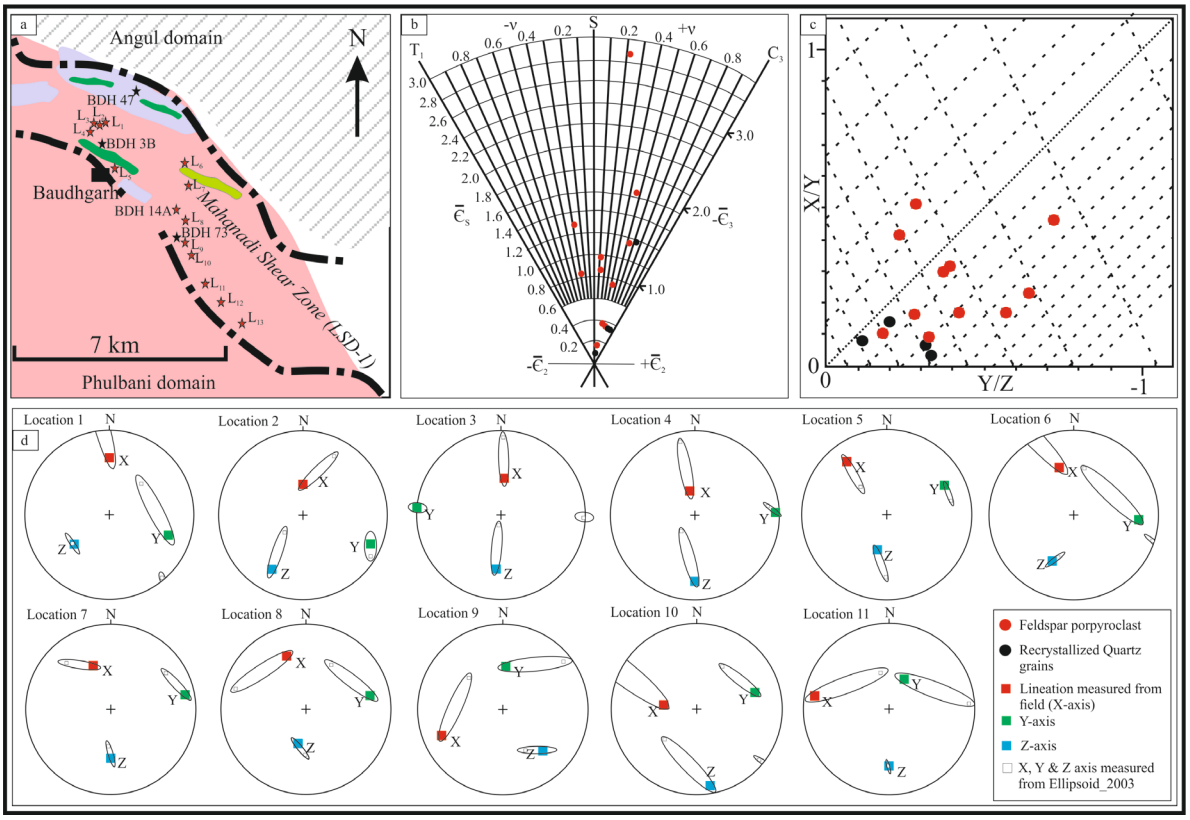

Figure 14: Map of the MSZ showing the locations of the sites and samples used for 3-D and 2-D finite strain estimation and for vorticity and EBSD analyses. (b) Representation of strain data in Hossack (1968) plot; (c) Representation of strain data in Flinn's (1962) diagram; (d) Stereographic plots showing close correspondence amongst the orientations of the three principal axes of the strain ellipsoid determined following the SPO-ELLIPSOID technique (Launeau and Robin, 2003b, 2005) at each location with actual foliation-lineation data measured from outcrops.

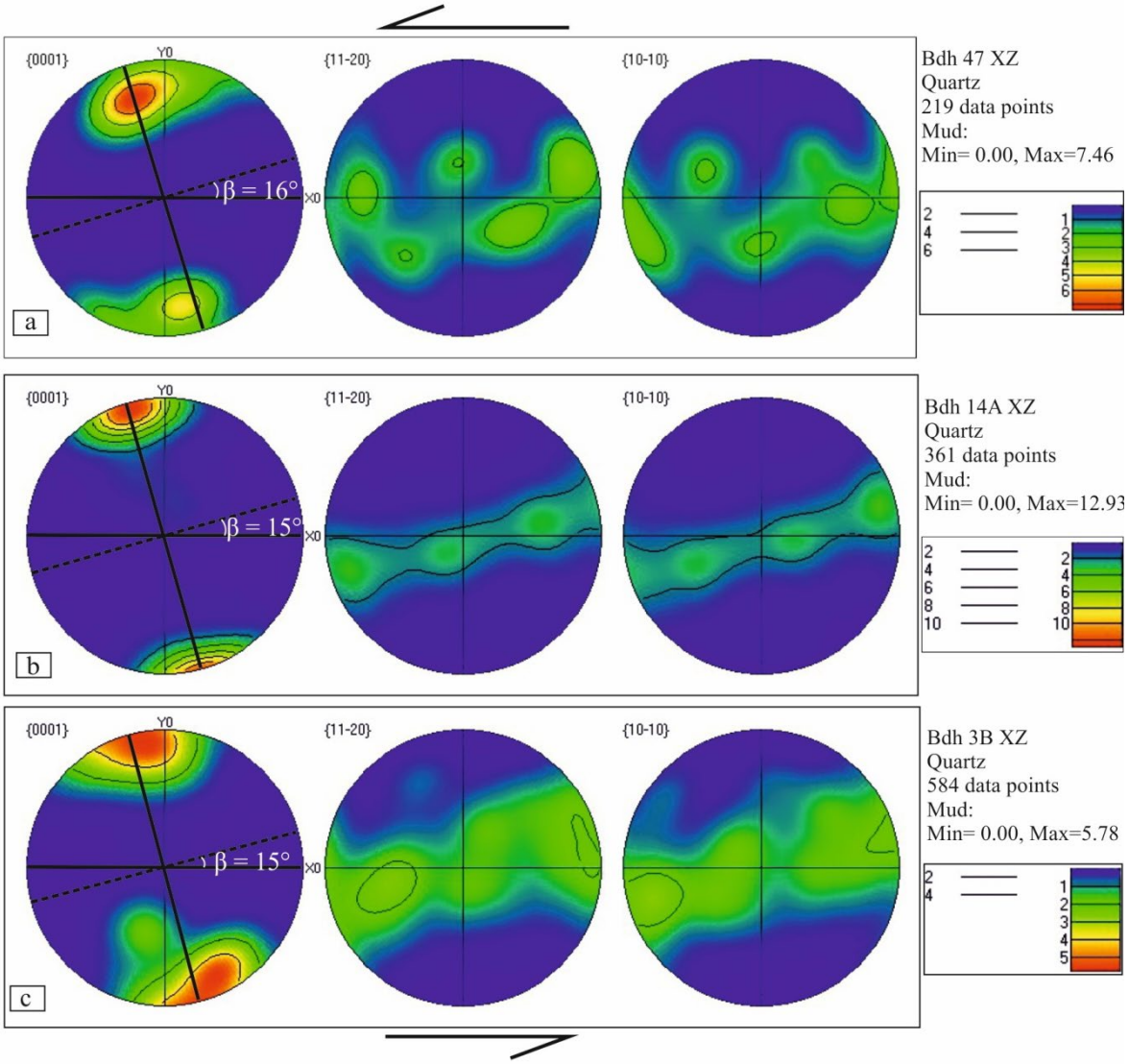

Figure 15: (a-c) Crystallographic orientation (CPO) of recrystallized quartz grains measured by Electron Backscatter Diffraction (EBSD) in XZ sections of finite strain ellipsoid from three samples (see Fig. 12a for sample locations; BDH 47-felsic gneiss, BDH 14A, and BDH 3B-augen gneiss). Equal area plots represent poles to base (0001) [c-axis], poles to the second order prism {11-20} <a-axes> and poles to the first order prism {10-10} <maxes>. The pole figure is plotted in lower hemisphere equal area projections, foliation oriented left-right and vertical with horizontal stretching lineation (X-direction). The vorticity angle (β) is shown in each plot. The arrows indicate the sense of shear determined from the inclination of the basal <a> slip system.

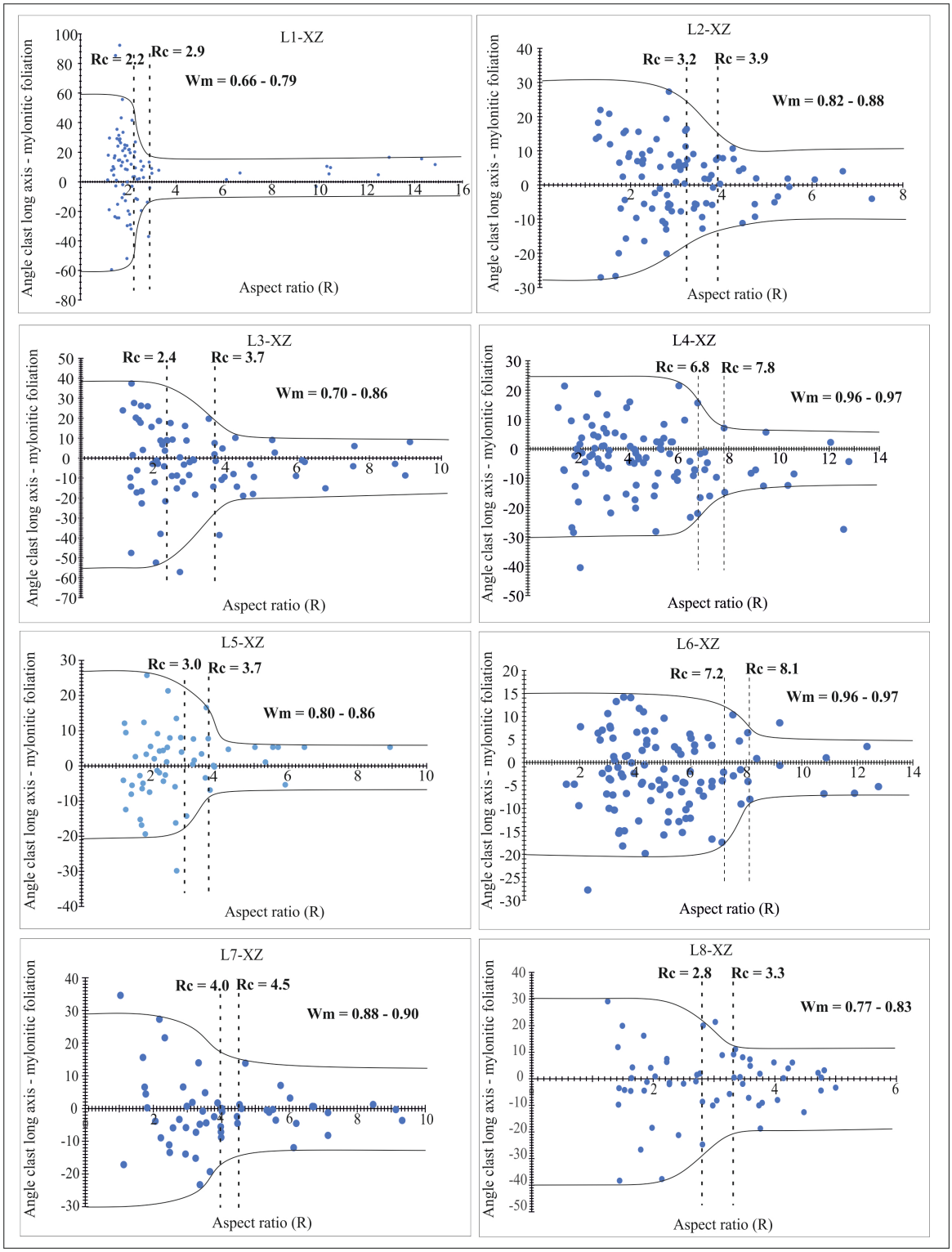

Figure 16: (a) Wallis' plots of feldspar porphyroclasts from mylonitic augen gneiss of the MSZ. The black-dash lines define the minimum and maximum critical shape ratio (Rc), its corresponding vorticity numbers determined by the rigid porphyroclast method from each site are also indicated in the figure. The site locations are shown in Figure 14(a).

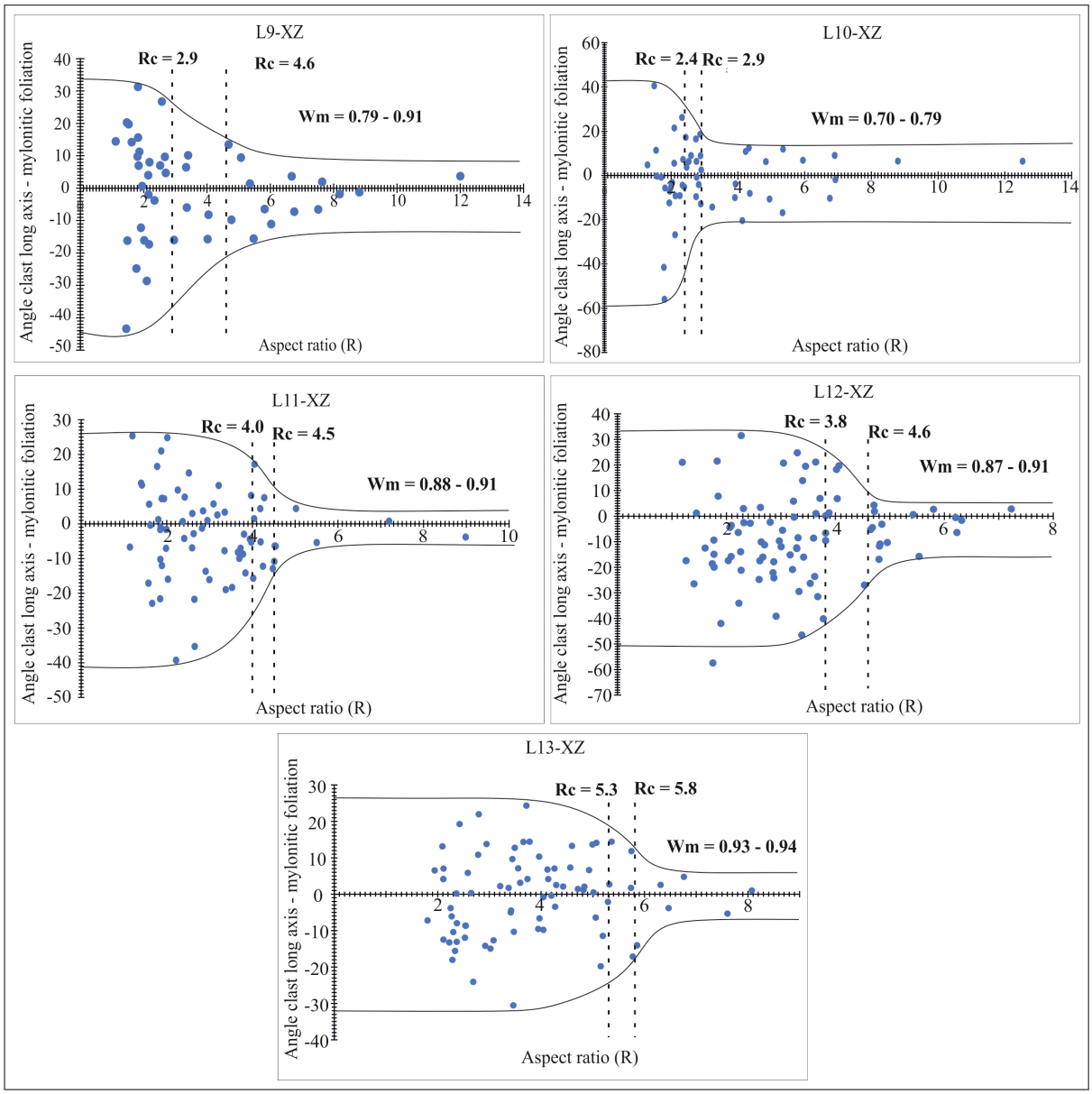

Figure 16: (b) Wallis' plots of feldspar porphyroclasts from mylonitic augen gneiss of the MSZ. The black-dash lines define the minimum and maximum critical shape ratio (Rc), its corresponding vorticity numbers determined by the rigid porphyroclast method from each site are also indicated in the figure. The site locations are shown in Figure 14(a).

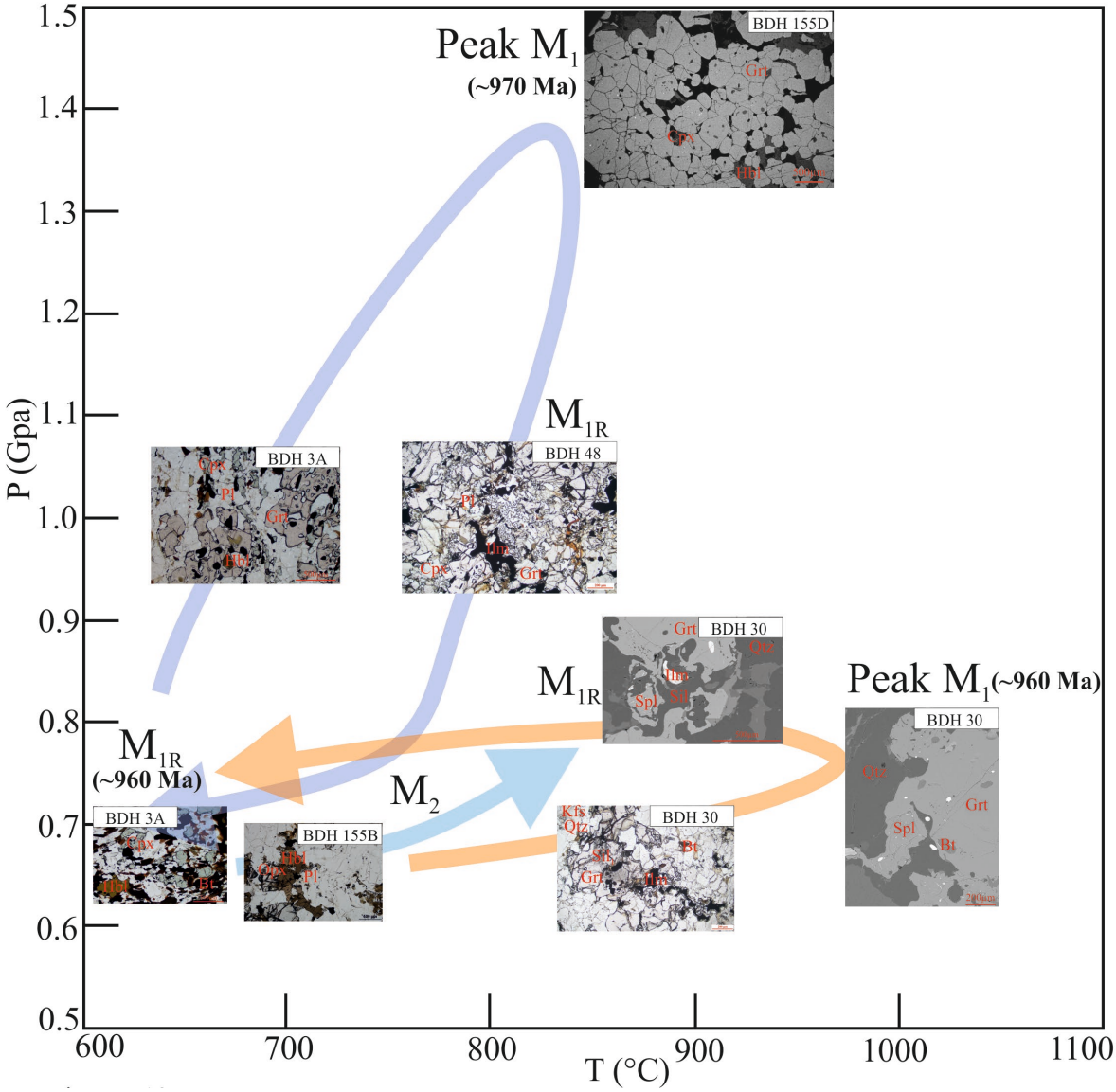

Figure 17: Constructed *P-T* paths of the rocks from the LSD-1 and LSD-2 based on texture, geothermobarometry, phase diagram modelling, and age data of representative samples. Note the contrasting *P-T* paths for the LSD-1 (blue line) and LSD-2 (orange line) rocks with clockwise and counterclockwise senses respectively.

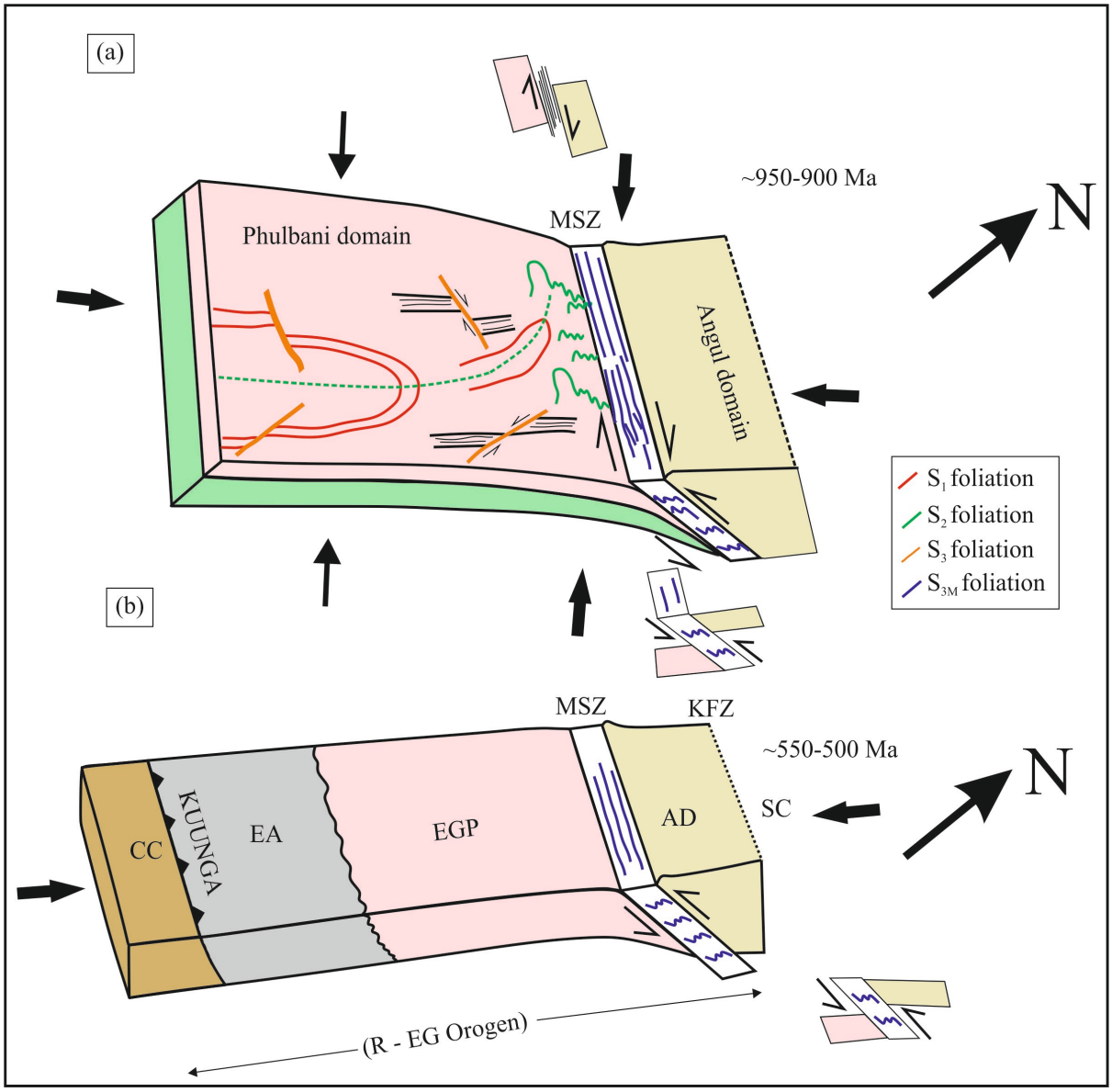

Figure 18: (a-b) Cartoon diagrams (Not to scale) illustrate kinematic models of MSZ and its footwall (Phulbani domain) at ca. 950–900 Ma (a) and 550–500 Ma (b).

Table 1: A summary of the sample description with sample numbers, GPS locations, mineral assemblages, important structures and textures along with calculated ages.

Rock name	Sample No.	GPS data	Mineralogy	Structures/ Textures	Other features	Age data
LSD-1: Samples from MSZ						
Grt-Cpx bearing mafic granulite	BDH 155D	20°52'24.80"N, 84°17'48.00"E	Grt+Cpx+Pl+Qtz+Hbl+Ilm+Rt	Massive to crudely foliated; granoblastic polygonal texture	Enclave within Opx-bearing mafic granulite, evidence of Hbl- dehydraion	
	BDH 48	20°52'1.00"N, 84°18'23.90"E	Grt+Cpx+Pl+Qtz+Ilm+Opx+Hbl+Bt	Massive, granoblastic polygonal texture; Symplectite of Cpx+ Pl+Opx after Grt	Enclave within mylonitized felsic gneiss	**1039-1019** Ma: Prograde M_1 age **967 ± 17** Ma: peak M_1 age **900 ± 13** Ma: M_2 age
	BDH 3A	20°51'10.10"N, 84°18'15.99"E	Grt+Cpx+Pl+Qtz+Ilm+Hbl+Bt+Opx	Massive, granoblastic polygonal texture	Enclave within mylonitized augen gniess; evidence of Hbl-dehydration melting	**956 ± 7** Ma: peak M_1 age **891 ± 23** Ma: M_2 age
Opx-bearing mafic granulite	BDH 155B	20°52'24.80"N, 84°17'48.00"E	Opx+Pl±Cpx+Hbl+Bt+Ilm+Qtz	Foliated, breakdown of Opx to Hbl and Hbl to Opx.	Enclave within mylonitized felsic gneiss	**1075-1001** Ma: Crystallization age **977 ± 12** Ma: peak M_1 age **904 ± 13** Ma- M_2 age
Hornblendite	BDH 77B	20°40'48.60"N, 84°32'54.90"E	Hbl+Pl+Kfs+Qtz+Ttn+Ilm	Massive to crudely foliated, foliation defined by Hbl	Enclave within mylonitized augen gniess	
Hornblende gneiss	T69	20°50'8.60"N, 84°19'46.00"E	Qtz+Pl+Hbl+Grt+Kfs+Ilm	Gneissic foliation shown by deformed Hbl	Enclave within mylonitized augen gneiss	**939 ± 11** Ma: crystallization age **885 ±12** Ma: M_2 age
Felsic gneiss	BDH 06	20°52'8.20"N, 84°18'16.40"E	Qtz+Kfs+Pl+Grt+Rt+Ms+Ilm+Bt	Mylonitic foliation	Occurs as lenses and fragments within mylonitized augen gneiss	**1242** Ma: xenocrystic core **964 ± 8** Ma: crystallization age **928-818** Ma: M_2 age
	BDH 13B	20°50'49.00"N, 84°18'57.00"E	Qtz+Kfs+Pl+Grt+Bt+Ilm	Mylonitic foliation	Occurs as lenses and fragments within mylonitized augen gneiss	
Augen gneiss	BDH 3B	20°51'10.10"N, 84°18'15.99"E	Qtz+Pl+Kfs+Grt+Ilm±Hbl+ Bt	Mylonitic foliation, Kfs and Pl porphyroclasts surounded by finer recrystallized grains	Host rock occupying the entire MSZ	**959 ± 8** Ma: crystallization age **914 ± 13** Ma: M_2 age
	BDH 16	20°49'43.30"N, 84°19'43.70"E	Qtz+Pl+Kfs+Grt+Ilm±Hbl+ Bt	Mylonitic foliation, Kfs and Pl porphyroclasts surounded by finer recrystallized grains	Host rock occupying the entire MSZ	
Hornblende granite	BDH 77A	20°40'48.60"N, 84°32'54.90"E	Qtz+Pl+Kfs+Hbl+Bt+Ilm	Mylonitic foliation defined by elongated Qtz-Hbl-Fs	Constitiutes a part of the host felsic gneiss	
LSD-2:Samples from south of MSZ						
Coarse-grained charnockite	BDH 62A	20°45'15.10"N, 84°12'49.90"E	Qtz+Pl+Kfs+Opx+Ilm+Bt	Massive to crudely foliated; foliation defined by elongated feldspar porphyroblasts	Intrusive, containing enclaves of mafic granulite	**978 ± 10** Ma: Crystallization age **959 ± 6** Ma: M_1 age
	BDH 152	20°43'60.00"N, 84°20'29.10"E	Qtz+Pl+Kfs+Opx+Grt+Ilm+Bt	Massive in nature	Intrusive, containing enclaves of mafic granulite	
Grt-Opx bearing mafic granulite	BDH 34D	20°41'47.50"N, 84°20'23.00"E	Grt+Opx+Pl+Kfs+Qtz+Bt+ Ilm	Granoblastic texture	Occurs as enclaves within coarse-grained charnockite	
	BDH 83C	20°41'37.90"N, 84°21'23.10"E	Opx+Pl+Ilm+Cpx+Grt+Qtz+Kfs	Granoblastic polygonal texture; Grt corona on Opx, Ilm and Pl along with Cpx	Occurs as enclaves within coarse-grained charnockite	
Aluminous granulite	BDH 30	20°43'32.10"N, 84°20'3.90°"E	Qtz+Kfs+Pl+Grt+Spl+Sil+Bt+Ilm	Corona of Sil+Grt over Spl	Occurs as lenses and fragments within pophyritic granite	**959 ± 8** Ma:M_1 age **894 ± 13** Ma: M_2 age
	BDH 34A	20°41'47.50"N, 84°20'23.00"E	Qtz+Kfs+Pl+Grt+Spl+Sil+Bt+Ilm	Foliated; foliation is defined by flat Qtz, Kfs, Sil, Grt and Spl	Occurs as lenses and fragments within pophyritic granite	**958 ± 15** Ma:M_1 age **899 ± 11** Ma: M_2 age
Calc-silicate granulite	BDH 62B	20°45'15.10"N, 84°12'49.90"E	Cpx+Pl+Wo+Grt+Ttn+Qtz+Cal	Gneissic foliation; Corona of Grt separating Cpx, Pl and Wo	Occurs as enclaves within coarse-grained charnockite	
Opx-bearing mafic granulite	BDH 28A	20°42'4.50"N, 84°27'11.60"E	Opx+Pl+Hbl+Ilm±Kfs±Qtz	Granoblastic texture of Opx, Pl and Ilm, massive rock	Occurs as enclaves within porphyritic granite	
Hornblende granite	BDH 40	20°50'3.20"N, 84°14'59.90"E	Qtz+Pl+Kfs+Grt+Ilm+Hbl+ Bt	Massive to crudely foliated, foliation defined by elongated feldspar	Constitutes a part of the host felsic gneiss	**947 ± 8** Ma: Crystallization age **894 ± 19** Ma: M_2 age
Augen gneiss	BDH 17B	20°48' 32.60"N, 84°13'56.20"E	Qtz+Pl+Kfs+Grt+Ilm+Bt	Mylonitic foliation	Occurs as a host gneiss	

Table 2: Summary of rock types, mineralogy, fabric types and deformation events of the studied rocks of the Phulbani domain (LSD-2) and the MSZ (LSD-1).

Rock types	Mineralogical/structural characters	Deformation phases
LSD-1 (MSZ)		
Augen gneiss	Mylonitic fabric (S_{3MH}) is defined by recrystallized Qtz, Kfs, Pl & layers of single elongated and small recrystallized Grt grains; S_{3ML} mylonitic fabric is defined by Chl + Bt.	D_{3MH} & D_{3ML}
Felsic gneiss	Mylonitic fabric (S_{3MH}) is defined by recrystallized Qtz, Kfs ribbons and elongated Grt + Ilm + Rt grains; S_{3ML} fabric is defined by retrogressed Bt grains.	D_{3MH} & D_{3ML}
Grt-bearing mafic granulite	Early mylonitic fabric (S_{3MH}) is defined by Hbl + Cpx + Opx and recrystallized Pl + Kfs + Qtz. S_{3ML} mylonitic fabric isdefined by small elongated Bt grains.	D_{3MH} & D_{3ML}
Cpx-bearing mafic granulite	Early mylonitic fabric (S_{3MH}) is defined by elongated and recrystallized Cpx and Hbl; S_{3ML} mylonitic fabric is defined by Bt along with recrystallized Qtz + Pl + Kfs grains.	D_{3MH} & D_{3ML}
LSD-2(Phulbani domain-MSZ footwall)		
Calc-silicate granulite	S_1 is defined by alternate greenish layer Cpx + Ttn + Qtz ± Pl ± Cal and greyish layer Cpx + Wo + Grt + Pl+ Ttn + Qtz + Cal	D_1
Aluminous granulite	Gniessic fabric (S_1) with alternate leucocratic layer (recrystallized Qtz + Kfs + Pl ± Sil) and mealonocratic layer (Grt + Sil + Spl + Ilm + Qtz); S_2 fabric defined by Sil grains.	D_1 & D_2
Felsic gneiss	S_1 is defined by Bt-rich layer; Gneissic fabric (S_2) is defined by alternate recrystallized Qtz + Kfs +P l and Bt-rich layer.	D_1 & D_2
Charnockite	Crudely foliated (S_2) id defined by elongated feldspar clasts.	D_2
Porphyritic granite	Well foliated (S_2) fabric is defined by recrystallized Qtz + Kfs + Pl and Grt + Bt + Ilm layer.	D_2

Table 3: A summary of vorticity data of feldspar porphyroclasts (~ 300 numbers from each sample) in mylonitic augen gneiss measured from thirteen sites across the MSZ. The sample locations are those used in Figure 14a.

Sample	XY plane	Axes value			Axes Orienatations			X/Z	X/Y	Y/Z								
		X(A) €1	Y(B) €2	Z (C) €3	X	Y	Z	A/C	A/B	B/C	K	√F (%)	€1	€2	€3	γ0	€s	ν
LSD-1 (MSZ)	Strain anlysis using field photographs of feldspar porpyroclasts determined by SPO-ELLIPSOID methodology																	
Location 1	320/45	1.59	1.09	0.58	360/33	109/27	230/45	2.76	1.46	1.89	0.52	6.1%	0.46	0.09	-0.55	0.52	0.39	0.27
Location 2	300/63	1.34	1.06	0.70	360/60	113/14	210/27	1.91	1.26	1.51	0.52	3.8%	0.29	0.06	-0.36	0.22	0.16	0.29
Location 3	275/54	1.47	1.20	0.57	005/54	275/00	185/36	2.59	1.23	2.11	0.21	9.9%	0.39	0.18	-0.56	0.50	0.37	0.56
Location 4	270/68	2.25	0.87	0.51	348/66	088/05	180/23	4.41	2.58	1.71	2.23	4.7%	0.81	-0.14	-0.67	1.12	0.84	-0.28
Location 5	285/35	2.10	1.06	0.45	323/23	63/25	195/55	4.67	1.99	2.35	0.73	6.2%	0.74	0.06	-0.79	1.18	0.88	0.11
Location 6	295/50	3.53	1.22	0.23	343/41	94/24	205/40	15.24	2.89	5.27	0.44	5.1%	1.26	0.20	-1.47	3.79	2.84	0.22
Location 7	270/48	2.01	1.36	0.37	338/44	79/12	180/42	5.50	1.48	3.71	0.18	3.3%	0.69	0.31	-0.99	1.55	1.16	0.55
Location 8	285/44	1.79	1.21	0.46	340/34	78/24	193/56	3.88	1.47	2.64	0.29	5.8%	0.58	0.19	-0.78	0.98	0.74	0.43
Location 9	230/57	2.73	0.84	0.44	247/23	004/48	136/33	6.27	3.25	1.93	2.41	0.4%	1.00	-0.17	-0.82	1.70	1.28	-0.29
Location 11	260/80	2.19	1.06	0.43	277/58	74/30	170/10	5.08	2.07	2.46	0.73	8.5%	0.78	0.06	-0.84	1.32	0.99	0.11
Location 13	270/56	2.33	1.37	0.31	280/13	27/58	180/34	7.45	1.70	4.38	0.21	4.4%	0.85	0.31	-1.17	2.19	1.64	0.47
LSD-1 (MSZ)	Strain anlysis using photomicrographs of recrystallized quartz grains by the SPO method																	
BDH 47	255/25	1.39	1.02	0.26				2.18	1.37	1.59	0.63		0.33	0.02	-1.35	1.59	1.19	0.63
BDH 14A	300/42	1.33	1.24	0.58				2.30	1.08	2.13	0.07		0.29	0.22	-0.54	0.42	0.32	0.83
BDH 73	260/46	1.23	1.02	0.79				1.56	1.20	1.30	0.67		0.21	0.02	-0.24	0.10	0.07	0.15
BDH 3B	260/50	1.39	1.20	0.58				2.40	1.16	2.07	0.15		0.33	0.18	-0.54	0.44	0.33	0.66

Table 4: Vorticity results obtained from quartz grains following oblique grain shape methods measured from the MSZ.

Sample	GPS Location	XY plane	X axis (plunge direction and plunge)	Rc	Wm	Pure shear (%)	Simple shear (%)
Location 1	20°51'12"N, 84°18'19"E	320/45	360/33	2.2-2.9	0.66-0.79	53-42	47-58
Location 2	20°51'12"N, 84°18'18"E	300/63	360/60	3.2-3.9	0.82-0.88	39-22	61-68
Location 3	20°51'12"N, 84°18'17"E	275/54	005/54	2.4-3.7	0.70-0.86	50-34	50-66
Location 4	20°51'11"N, 84°18'17"E	270/68	348/66	6.8-7.8	0.96-0.97	19-17	81-83
Location 5	20°51'01"N, 84°18'35"E	285/35	323/23	3.0-3.7	0.80-0.86	51-34	49-66
Location 6	20°50'8.94"N, 84°19'45.98"E	295/50	343/41	7.2-8.1	0.96-0.97	19-17	81-83
Location 7	20°50'07"N, 84°19'46"E	270/48	338/44	4.0-4.5	0.88-0.90	31-28	69-72
Location 8	20°49'44"N, 84°19'50"E	285/44	340/34	2.8-3.3	0.77-0.83	44-37	56-63
Location 9	20°48'55"N, 84°19'36"E	230/57	247/23	2.9-4.6	0.79-0.91	41-27	59-73
Location 10	20°48'47"N, 84°19'39"E	265/75	275/32	2.4-2.9	0.70-0.79	50-42	50-58
Location 11	20°48'25"N, 84°19'47"E	260/80	277/58	4.0-4.5	0.88-0.91	31-27	69-73
Location 12	20°48'16"N, 84°19'49"E	270/52	288/21	3.8-4.6	0.87-0.91	32-27	68-73
Location 13	20°48'8.10"N, 84°19'51.80"E	270/56	280/13	5.3-5.8	0.93-0.94	25-23	75-77